

Thesis Title

by

E. Ross



A thesis submitted to the
University of Birmingham
for the degree of
DOCTOR OF PHILOSOPHY

Solar and Stellar Physics Group (SASP)

School of Physics and Astronomy

University of Birmingham

Birmingham, B15 2TT

Month 20XX

Contents

List of Figures	v
List of Tables	vi
List of Abbreviations	vii
1 A Frequency Domain Investigation on the Morphology of the Solar Mean Magnetic Field	1
1.1 Introduction	1
1.2 Aims	5
1.3 Data	6
1.3.1 Summary of the Data Set	6
1.3.2 Obtaining the SMMF from BiSON	7
1.4 Methodology	10
1.4.1 Identifying Features in the SMMF Power Spectrum	10
1.4.2 Parametrisation of the SMMF Power Spectrum	13
1.4.3 Modelling the SMMF Power Spectrum	15
1.4.4 Comparison with the WSO SMMF	16
1.5 Results	17
1.5.1 Investigation of the Window Function	17
1.5.2 Modelling the BiSON Power Spectrum	22
1.5.3 Comparison to the WSO Power Spectrum	26
1.6 Discussion	30
1.6.1 Testing the Effects of Differential Rotation and Active Region Migration	30
1.6.2 Further Morphology of the SMMF using SDO/HMI Data	34
1.7 Conclusion	36
2 Rossby Modes in the Solar Mean Magnetic Field	40
2.1 Introduction	40
2.2 Theory	42
2.3 Methodology	44
2.3.1 Testing the Residual Spectrum	44
2.3.2 Modelling r mode Profiles	47
2.4 Results	48
2.4.1 Testing the Residual Spectrum	48
2.4.2 Modelling r mode Profiles	50

2.5	Discussion	52
2.5.1	Manifestation of Rossby Waves in the Power Spectrum	52
2.5.2	Rossby Modes in Other Sources of SMMF Data	56
2.6	Conclusion	58
Bibliography		60

List of Figures

1.1	An example of the BiSON ratios data over a 30-minute period. The separation between the two ratios is due to the solar mean magnetic field. Other excursions in the individual ratios are due to the other effects measured by the RSS.	9
1.2	(a) 40-second cadence observations of the SMMF from the Sutherland BiSON station between 1992 and 2012. The sense of the field was chosen to match the Chaplin et al. (2003) and the WSO observations, where positive is for a field pointing outwards from the Sun. (b) Power spectrum of the SMMF on a 40-second cadence truncated to $10\mu\text{Hz}$, however, the Nyquist frequency is $12500\mu\text{Hz}$	11
1.3	Power spectrum of 40-second cadence SMMF from the Sutherland BiSON station observed between 1992 – 2012 on a logarithmic scale up to the Nyquist frequency.	12
1.4	Locations of aliased power in side-band peaks. The orange, dotted-lines show the locations of frequencies at multiples of 1/day. The green, dashed-lines show the locations of the side-band peaks – harmonic frequencies reflected around multiples of 1/day. The inset shows a zoom of one set of side-band peaks around 1/day.	18
1.5	The effects of the window function on the power spectrum is shown by using a fake data set and this is compared to the BiSON power spectrum. Black line: BiSON SMMF PSD; blue line: power spectrum of the window function; green and dark-orange lines: the power spectrum of the artificial data without and with gaps, respectively; light orange line: the input peak used to generate the artificial data over-plotted. The power spectra of the BiSON SMMF and the window function have been shifted upwards by a factor of 6 and 30, respectively, for clarity.	20
1.6	Full, modelled power spectrum of the BiSON SMMF on logarithmic axes. The data are displayed in black and the convolved model using symmetric Lorentzian peaks is shown in green.	25
1.7	Modelled power spectrum of (a) the WSO SMMF; (b) the daily-averaged BiSON SMMF, on logarithmic axes. The data are displayed in black and the convolved model using asymmetric Lorentzian peaks is shown in blue and green, for WSO and BiSON, respectively.	28

1.8	A comparison between the power spectra produced using the daily averaged BiSON data and the 40-second cadence BiSON observations. The top plot shows the log-smoothed power spectra of the daily averaged data (blue) and the 40-second data (orange). The bottom panel show the ratio of the daily averaged data power spectrum to the 40-second data power spectrum. The horizontal, dashed line indicates a ratio of 1.	29
1.9	(a) Shows the Lorentzian distribution peak before and after the time-averaged broadening, and the fit to the broadened peak. (b) Shows the peak distribution before and after the analytical broadening, and the fit to the broadened peak. In both plots the broadened peaks have been shifted by the relevant frequency to overlay them on top of the true ν_0 for comparison.	34
1.10	Investigations of timescales in the SDO/HMI magnetograms over 2011 and 2014. Both plots show in the top panel, the hemispheric Mean Magnetic Field (MMF) and full-disc Solar Mean Magnetic Field (SMMF) from the magnetograms. The lower panel of each plot displays a comparison between the hemispheric and full-disc mean of the synoptic charts, compared to the box-car smoothed MMF from the magnetograms. N: Northern hemisphere; S: Southern hemisphere. Full HMI: considers the full solar disc; 99 HMI: considers only the inner 99% of the solar disc, by radius.	35
2.1	Full, modelled power spectrum of the BiSON SMMF on logarithmic axes. The data is displayed in black and the convolved model using symmetric Lorentzian peaks is shown in green.	42
2.2	Residual power spectrum of the BiSON SMMF. Over plotted in the dark blue curve is the model of the main SMMF signal which was divided out from the raw spectrum. Also over plotted as vertical solid lines are the expected locations of the 4 lowest-frequency sectoral r modes and the dashed lines, the locations of the B_0 variation frequency splitting. Dashed lines represent ± 31.7 nHz (i.e. representing the frequencies of splitting due to the variation in the B_0 angle.) . . .	45
2.3	Realisations of the statistics tests on the BiSON data for different re-binning factors (n). The panels of each sub figure are: (top) the full PSD and fit, (second panel) the full and re-binned residuals, (third panel) the probability of statistical noise in each bin, (bottom) distribution of the residuals compared to a χ^2 $2n$ -DOF.	49
2.4	Model fit to the r mode in the BiSON PSD residuals using the median values from the posterior distributions of each parameter.	51
2.5	Mode displacement schematic for an $l = m = 2$ r mode (Strohmayer & Mahmoodifar, 2014)	53

2.6	Time series of the velocity and amplitude modulation toy model simulations. The blue curve shows the velocity modulation, i.e. modulating using a cosine with period of 1 year, whereas the orange curve shows the amplitude modulation, i.e. modulating using a rectified cosine with period 1 year.	54
2.7	Power spectra for the two modulation methods, showing the difference in the way the modulation has changed the frequency of the observed mode.	54
2.8	SDO/HMI SMMF split into hemispheres and compared to other SMMF sources during (a) 2011, and (b) 2014. The top panel in each figure shows the north (N), south (S), and total disc-averaged mean magnetic field, for both the full solar disc and from pixels within 99% of solar radius. The bottom panels show a comparison between the SMMF, as observed BiSON, WSO, and SDO/HMI (full disc and the 99% disc).	55
2.9	Comparison of the power spectra for BiSON, WSO, and SDO/HMI. In both figures, the top panel shows the BiSON PSD and the bottom panel shows either the WSO or HMI PSD. The dashed, black line shows the location of the theoretical $l = 2 = m$ r mode frequency, and the red, solid line shows the location of the peak fit in the BiSON PSD residuals.	57

List of Tables

1.1	Model parameter values for the generation of artificial data, and the median posterior values for the fit to the power spectra generated with and without the gaps in the data. Numbers in brackets denote uncertainties on the last 2 digits, and all uncertainties correspond to the 68% credible intervals either side of the median.	21
1.2	Median values of the marginalised posterior distributions for each model parameter in the fit to the BiSON power spectrum using symmetric and asymmetric Lorentzian profiles. Numbers in brackets denote uncertainties on the last 2 digits, and all uncertainties correspond to the 68% credible intervals either side of the median in the adjusted posteriors. The last row in the table shows the Bayesian Information Criterion (BIC) value for each model.	24
1.3	Median values of the marginalised posterior distributions for each model parameter in the fit to the daily WSO and BiSON power spectra. Numbers in brackets denote uncertainties on the last 2 digits, and all uncertainties correspond to the 68% credible intervals either side of the median. The last row in the table shows the BIC value for each model.	28
1.4	Input linewidth and the median posterior values of the Lorentzian model each simulation. Numbers in brackets denote uncertainties on the last 2 digits, and all uncertainties correspond to the 68% credible intervals either side of the median.	33
2.1	Predicted ⁺ and observed ^o r mode frequencies for combinations of l and m . Predicted frequencies and conversions of observations to different frames of reference use equation (2.1), equation (2.2), and equation (2.3), with $\Omega = 453.1$ nHz. The predicted splitting for the B_0 angle variation is also provided. The key for the source column is: LPT for Löptien et al. (2018), LNG for Liang et al. (2019), and LZA for Lanza et al. (2019).	44
2.2	Median posterior values of the Lorentzian model for the r mode peak in the BiSON SMMF PSD. Numbers in brackets denote uncertainties on the last 2 digits, and all uncertainties correspond to the 68% credible intervals either side of the median.	50

List of Abbreviations

AR Active Region.

BIC Bayesian Informatin Criterion.

BiSON Birmingham Solar Oscillations Network.

EEMD Empirical Mode Decomposition.

FA False Alarm.

GMF General Magnetic Field.

HMC Hamiltonian Monte Carlo.

LOS Line Of Sight.

MCMC Markov Chain Monte Carlo.

MFC Magnetic Flux Concentration.

MMF Mean Magnetic Field.

NUTS No U-Turn Sampler.

PSD Power Spectral Density.

RM Rotationally Modulated.

RMS Root Mean Square.

RSS Resonant Scattering Spectrometer.

SB Stochastic Background.

SDO/AIA Solar Dynamics Observatory Atmospheric Imaging Assembly.

SDO/HMI Solar Dynamics Observatory Helioseismic and Magnetic Imager.

SMMF Solar Mean Magnetic Field.

SOHO/MDI Solar and Heliospheric Observatory Michelson Doppler Imager.

WSO Wilcox Solar Observatory.

1 A Frequency Domain Investigation on the Morphology of the Solar Mean Magnetic Field

1.1 Introduction

The Sun has a complicated magnetic field structure; many features of the Sun and proxies for the solar activity are related to the evolution of the Sun's magnetic field (Wu et al., 2018).

The Solar Mean Magnetic Field (SMMF) is a surprising, non-zero measurement of the imbalance of opposite magnetic flux polarities observed on the full, visible disc of the Sun (Svalgaard et al., 1975), and is defined as the mean Line Of Sight (LOS) magnetic field when observing the Sun-as-a-star (Scherrer et al., 1977a,b; Garca et al., 1999). In the literature the SMMF is also sometimes referred to as the General Magnetic Field (GMF) (Severny, 1971) or the Mean Magnetic Field (MMF) (Kotov, 2008) of the Sun.

Observations of the SMMF have typically been made by measuring the Zeeman splitting of spectral lines using a ground-based Babcock-type magnetograph (Scherrer et al., 1977a), although more recently the SMMF has been calculated from full-disc LOS magnetograms taken from space-borne telescopes such as the Solar Dynamics Observatory Helioseismic and Magnetic Imager (SDO/HMI), in order to

understand the morphology of the SMMF (Kutsenko et al., 2017; Bose & Nagaraju, 2018). It is understood that the strength of the SMMF may vary depending on the spectral line used to measure the SMMF (Kotov, 2008, 2012), however, it is generally accepted in the literature that the SMMF varies slowly with the solar activity cycle, with an amplitude of around ± 2 G during solar maximum and around ± 0.2 G during solar minimum (Plachinda et al., 2011). In addition, the SMMF displays a strong, quasi-coherent rotational signal, which must arise from inhomogeneities on the solar disc with lifetimes of several rotations (Chaplin et al., 2003; Xie et al., 2017).

Despite existing literature on SMMF observations spanning several decades, ultimately, the origin of the SMMF remains an open question in solar physics. The principle component of the SMMF is commonly assumed to be weak, large-scale magnetic flux, distributed over vast areas over the entire solar disc, rather than from more concentrated regions such as Active Regions (ARs) or sunspots (Severny, 1971; Scherrer et al., 1977a; Xiang & Qu, 2016). However, conversely, Scherrer et al. (1972) found that the SMMF was most highly correlated with flux from only the inner-most one quarter, by area, of the solar disc, which is more sensitive to active latitudes.

In recent literature, Bose & Nagaraju (2018) provided a novel approach to understanding the SMMF whereby they decomposed the SMMF through feature identification and pixel-by-pixel analysis of full-disc magnetograms. Bose & Nagaraju (2018) concluded that: (i) the observed variability in the SMMF lies in the polarity imbalance of large-scale magnetic field structures on the visible surface of the Sun, (ii) the correlation between the flux from sunspots and the SMMF is statistically insignificant, (iii) and more critically that the background flux dominates the SMMF, accounting for around 89% of the variation in the SMMF. However, there still remained a strong manifestation of the rotation in the background magnetic field presented by Bose & Nagaraju (2018). This is indicative of inhomogeneous

magnetic features with lifetimes on the order of several solar rotations rather than the shorter-lived, weaker fields usually associated with the large-scale background. It therefore raises the question of whether their technique assigned flux from Magnetic Flux Concentrations (MFCs) or ARs to the background.

In order to identify the contours of specific features [Bose & Nagaraju \(2018\)](#) used an adaptive thresholding technique on various Solar Dynamics Observatory Atmospheric Imaging Assembly (SDO/AIA) images of the solar disc to create binary masks for different types of features. These masks were then applied to scaled SDO/HMI magnetograms in order to separate the features on the disc and their contribution to the SMMF. Upon a closer inspection of the example magnetogram in Figure 2 of the paper, with over-plotted contours of identified features from SDO/AIA images, there are clearly regions of strong MFCs in the local vicinity of, and connected to, the identified features that lie outside their contour lines and are therefore allocated to the background magnetic field, rather than attributed to the specific features. It seems an obvious statement to suggest that SDO/AIA optical counterparts of the magnetograms will not exactly align with the observed magnetic flux in the magnetograms. We expect that the magnetic field will manifest itself differently in the optical observations and the magnetograms, which leads one to believe that the background component in this study could mistakenly contain flux from some of the identified features.

In particular, in their example plot, the contours for sunspots typically only cover the umbra, not accounting for the surrounding penumbra. It is not clear whether this will have a large effect, but certainly we expect that some strong magnetic flux associated with sunspots has been attributed to the background, or other nearby features. One other note; there was a treatment of plages in this work, from additional chromospheric observations, but a separate, specific handling of faculae in the photosphere was absent. Incorporating this could have contributed to the completeness of the study. Furthermore, a decomposition of the identified

background component into regimes of strong and weak field would have provided more clarity on the exact morphology of the SMMF, and would have likely provided evidence to conclude whether flux from AR features were, in fact, incorporated into the background.

Despite these findings, it is known that the strength of the SMMF is weaker during solar minimum, when there are fewer ARs, and stronger during solar maximum, when there are more ARs. This is suggestive that the evolution of ARs has relevance for the evolution of the SMMF.

There is a contrasting view in the literature which suggests AR flux dominates the SMMF. [Kutsenko et al. \(2017\)](#) claim that a large component of the SMMF may be explained by strong and intermediate flux regions. These regions are associated with ARs; using a thresholding technique they showed between 65% to 95% of the SMMF could be attributed to strong and intermediate flux, while the fraction of the occupied area varied between 2% to 6% of the disc area, depending on the chosen threshold for separating weak and strong flux. This finding suggests that strong, long-lived, inhomogeneous MFCs produce the strong rotation signal in the SMMF. Potential sources could be sunspots, plages, faculae, etc. and [Kutsenko et al. \(2017\)](#) discussed that there is an entanglement of strong flux (typically associated with ARs) and intermediate flux (typically associated with network fields and remains of decayed ARs). Disentangling the flux would have provided a more accurate analysis of the SMMF owing to a clearer picture of the main contributor to the SMMF.

The Sun's dynamo and hence magnetic field is directly coupled to the solar rotation. The Sun exhibits latitude-dependent and depth-dependent differential rotation with a sidereal, equatorial period of around 25 days ([Howe, 2009](#)). To Earth-based observers, the synodic rotation of the Sun is observed at around 27 days, and the SMMF displays a dominant periodicity of around 27 days due to the solar rotation ([Chaplin et al., 2003](#); [Xie et al., 2017](#); [Bose & Nagaraju, 2018](#)). It was also reported by [Xie et al. \(2017\)](#) that the differential solar rotation was observed in the

SMMF with measured rotational periods of 28.28 ± 0.67 days and 27.32 ± 0.64 days for the rising and declining phases, respectively, of all of the solar cycles in their considered time-frame.

On the other hand, [Xiang & Qu \(2016\)](#) utilised ensemble Empirical Mode Decomposition (EEMD) analysis to extract rotational modes in the SMMF and found two rotation periods which are derived from different strengths of magnetic flux elements. They found that a rotation period of 26.6 days was related to a weaker magnetic flux element within the SMMF, while for stronger magnetic flux elements in the SMMF, the measured rotation period was 28.5 days.

Ultimately, to date, our understanding of the SMMF and its origin remains rather limited.

1.2 Aims

In this work an investigation of high-cadence (sub-minute) observations of the SMMF, made by Birmingham Solar Oscillations Network (BiSON) ([Chaplin et al., 1996, 2005](#); [Hale et al., 2016](#)), was performed. The aim of the investigation was to understand the morphology of the SMMF.

This work provides a frequency domain analysis of the SMMF data, where a model was built and fit to the power spectrum of the SMMF which allowed us to understand the characteristics of its source(s).

The Rotationally Modulated (RM) signal in the SMMF was clearly observed as several low-frequency peaks in the power spectrum. In addition, the use of the high-cadence data was especially crucial for inferences on components of the SMMF with periods of less than a day at higher frequencies in the power spectrum, with the intention to determine whether the background magnetic field exhibited a stochastically excited component, which evolved on short timescales.

1.3 Data

1.3.1 Summary of the Data Set

Chaplin et al. (2003) provided the first examination of the SMMF using data from BiSON, and the work presented in this paper is a continuation of that study.

BiSON is a six-station, ground-based, global network of telescopes continuously monitoring the Sun, which principally makes precise measurements of the LOS velocity of the photosphere due to solar p mode oscillations (Hale et al., 2016). Through the use of polarising optics and additional electronics, the BiSON spectrometers can measure both the disc-averaged LOS velocity and magnetic field in the photosphere (Chaplin et al., 2003), however, not all BiSON sites measure the SMMF.

In this study we focus on the data collected by the Sutherland node, in South Africa, which was also used by Chaplin et al. (2003). Data are sampled on a 40-second cadence, and the SMMF data collected by the Sutherland station pertains the epochs from 01/1992 – 12/2012 (i.e. covering 7643 days). Over this period, the fill of solar observations is low because of the combination of: (a) the fill due to using only a single site with a 40-second cadence, (b) the duty cycle needed in a given day for a ‘good measure’ of the Sun. Combined, the fill of the data is $\sim 15.6\%$ of the total epoch. If instead we take a daily average of the BiSON SMMF, the average duty cycle is $\sim 55.2\%$. This gives a higher duty cycle but a lower Nyquist frequency. Because of the much lower Nyquist frequency, modelling the background power spectral density is more challenging; therefore we use the 40-second cadence data in this work.

As a comparison to the BiSON data, SMMF observations were also acquired by the Wilcox Solar Observatory (WSO) (<http://wso.stanford.edu/>) (Scherrer et al., 1977b). The WSO SMMF data are sampled daily from 16/05/1975 – present day, but for comparison with the BiSON SMMF, we only used data over the same temporal range.

The WSO also measures the LOS SMMF using a Babcock-type magnetograph, which allows the measurement of the amount and sense of circular polarisation in the wings in an absorption line (Scherrer et al., 1977a). WSO uses two absorption lines for the measurement of the magnetic field: the Fe I at 5250 Å ($\lambda 5250$) is used for measurement of the field, and Fe I at 5124 Å ($\lambda 5124$) is used to determine the instrument’s zero offset, as this line is magnetically insensitive. Scherrer et al. (1977a) describes that a single, complete observation takes ~ 20 minutes, consisting of four 3-minute integrations. The data provided by WSO are a daily weighted mean of the observations, where the weighting used is the statistical uncertainty and the magnitude of the zero offset measured with the $\lambda 5124$ line.

1.3.2 Obtaining the SMMF from BiSON

There is no catalogued BiSON SMMF data-set, so it was necessary to compute the SMMF from the available BiSON data. To acquire the SMMF from BiSON data, the method as described by Chaplin et al. (2003) was adopted; here we discuss the key aspects.

Each BiSON site employs a Resonant Scattering Spectrometer (RSS) to measure the Doppler shift of the $^2S_{1/2} \rightarrow ^2P_{1/2}$ line (D1 line) of potassium, at ~ 770 nm (Brookes et al., 1978). A potassium vapour cell placed within a longitudinal magnetic field Zeeman splits the laboratory line into the two allowed D1 transitions (Lund et al., 2017). The intensity of the longer wavelength (red; I_R) and shorter wavelength (blue; I_B) components of the line may be measured by the RSS almost simultaneously, by using polarising optics to switch between the red and blue wings of the line, to form the ratio given by equation (1.1), which is used as a proxy for the Doppler shift from the LOS velocity of the photosphere (see: Brookes et al., 1976, 1978; Elsworth et al., 1995a; Chaplin et al., 2003; Lund et al., 2017):

$$\mathcal{R} = \frac{I_B - I_R}{I_B + I_R}. \quad (1.1)$$

Photospheric magnetic fields Zeeman split the Fraunhofer line and the Zeeman-split components have opposite senses of circular polarization (Chaplin et al., 2003). Additional polarising optics are used in the RSS to manipulate the sense of circular polarization (either + or -) that is passed through the instrument. The ratio \mathcal{R}_+ or \mathcal{R}_- is formed, and the ratios \mathcal{R}_\pm would be equal if there was no magnetic field present.

The observed ratio (\mathcal{R}_\pm) may be decomposed as:

$$\mathcal{R}_\pm = \mathcal{R}_{\text{orb}} + \mathcal{R}_{\text{spin}} + \mathcal{R}_{\text{grs}} + \delta r_{\text{osc}}(t) \pm \delta r_B(t). \quad (1.2)$$

where \mathcal{R}_{orb} is due to the radial component of the Earth’s orbital velocity around the Sun, $\mathcal{R}_{\text{spin}}$ is due to the component towards the Sun of the Earth’s diurnal rotation about its spin axis as a function of latitude and time, \mathcal{R}_{grs} is from the gravitational red-shift of the solar line due to the Sun’s mass (Elsworth et al., 1995b; Dumbill, 1999), $\delta r_{\text{osc}}(t)$ is due to the LOS velocity of p mode oscillations, and $\delta r_B(t)$ is due to the magnetic field (\pm denotes the polarity of the Zeeman-split line that is being observed) (Dumbill, 1999).

The effect of the magnetic field on the ratio is shown in Fig. 1.1, and it is clear to see from equation (1.3) that the difference between the opposite magnetic field ratios is twice the magnetic ratio residual, i.e.:

$$\mathcal{R}_+ - \mathcal{R}_- = 2 \delta r_B(t). \quad (1.3)$$

The BiSON RSS is measuring the velocity variation on the solar disc, and therefore a calibration from the ratio to a velocity is necessary. One method of velocity calibration is achieved by first fitting the daily observed ratio, averaged over both magnetic polarities, to a 2nd- or 3rd-order polynomial as a function of velocity, as discussed by Elsworth et al. (1995b). Here we chose to fit the ratio in terms of velocity, $\mathcal{R}_{\text{calc}}(u)$, i.e.:

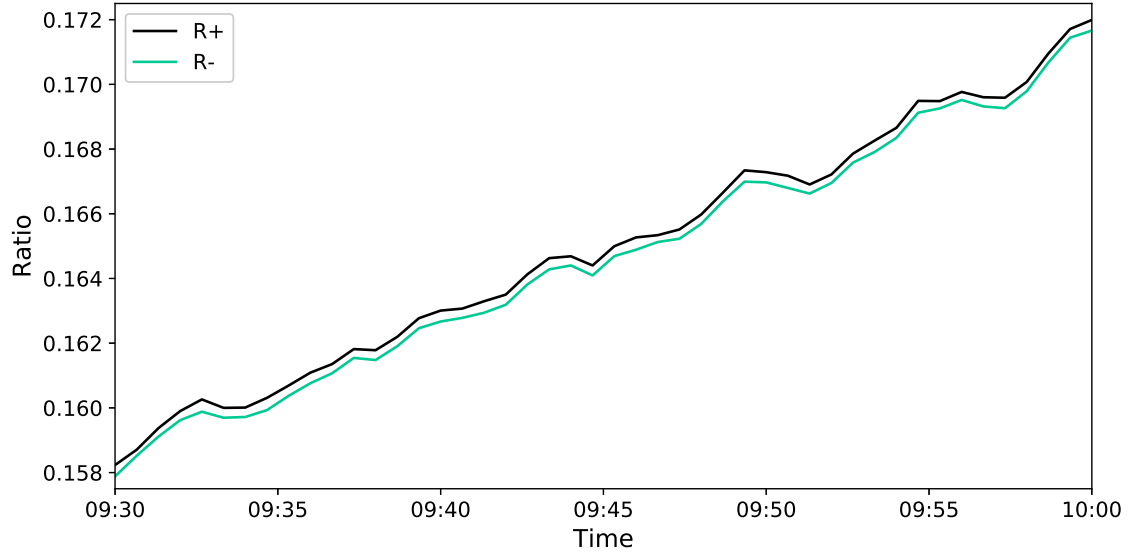


Figure 1.1: An example of the BiSON ratios data over a 30-minute period. The separation between the two ratios is due to the solar mean magnetic field. Other excursions in the individual ratios are due to the other effects measured by the RSS.

$$\mathcal{R}_{\text{calc}}(u) = \sum_n \mathcal{R}_n u^n, \quad (1.4)$$

where:

$$u = v_{\text{orb}} + v_{\text{spin}}, \quad (1.5)$$

and v_{orb} is the velocity component related to the ratio, \mathcal{R}_{orb} ; v_{spin} is related to the ratio, $\mathcal{R}_{\text{spin}}$; and n is the polynomial order.

It is possible to see that through the removal of $\mathcal{R}_{\text{calc}}(u)$ from the observed ratios, one is left with the ratio residuals of the p mode oscillations and the magnetic field, i.e.:

$$\mathcal{R}_{\pm} - \mathcal{R}_{\text{calc}}(u) = \delta r_{\text{osc}}(t) \pm \delta r_{\text{B}}(t). \quad (1.6)$$

Furthermore, conversion from ratio residuals into velocity residuals uses the calibration given by:

$$\delta v(t) = \left(\frac{d\mathcal{R}_{calc}}{dV} \right)^{-1} \delta r(t). \quad (1.7)$$

In order to finally obtain the SMMF in units of magnetic field, one must combine equation (1.3) and equation (1.7) with the conversion factor in equation (1.9) (Dumbill, 1999), and the entire procedure can be simplified into:

$$B(t) = \frac{1}{2} \left(\frac{d\mathcal{R}_{calc}}{dV} \right)^{-1} \frac{(\mathcal{R}_+ - \mathcal{R}_-)}{K_B}, \quad (1.8)$$

where:

$$K_B = \frac{8}{3} \frac{\mu_B}{h} \frac{c}{\nu} \approx 2.89 \text{ ms}^{-1} \text{ G}^{-1}, \quad (1.9)$$

and μ_B is the Bohr magneton, h is Planck's constant, c is the speed of light, and ν is the frequency of the photons.

Through the application of this methodology, one acquires the SMMF as shown in Fig. (1.2a). The power spectrum of the full, 7643-day Sutherland data set is shown in Fig. (1.2b), and it shows a strong rotational signal at a period of ~ 27 days.

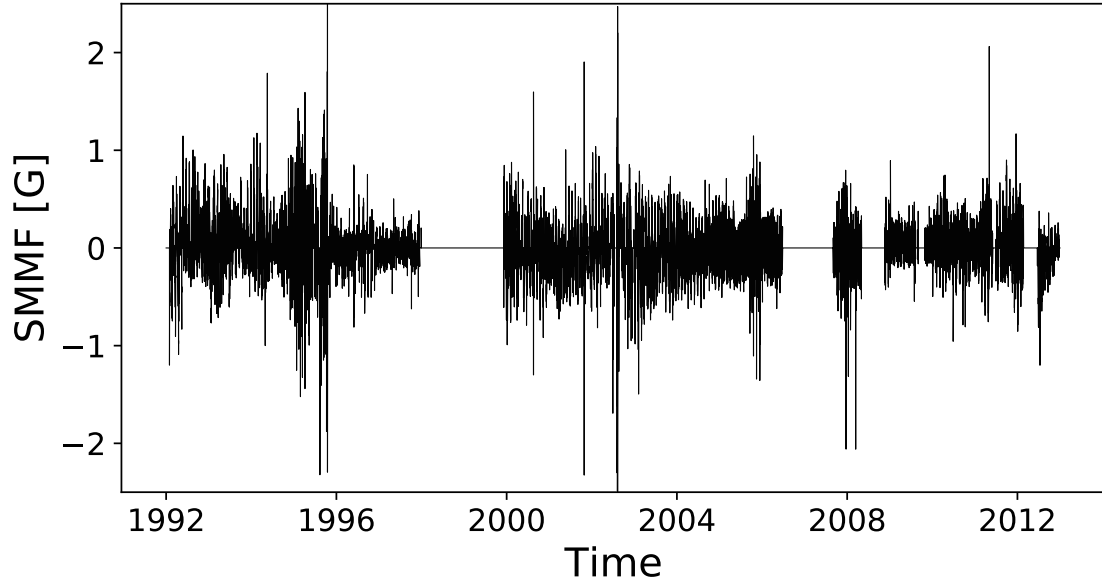
The power spectrum shows a clear set of strong peaks at low frequency, which are due to the persistent rotation signal in the SMMF. The largest peak is the fundamental rotation frequency, and the following peaks are its harmonics.

1.4 Methodology

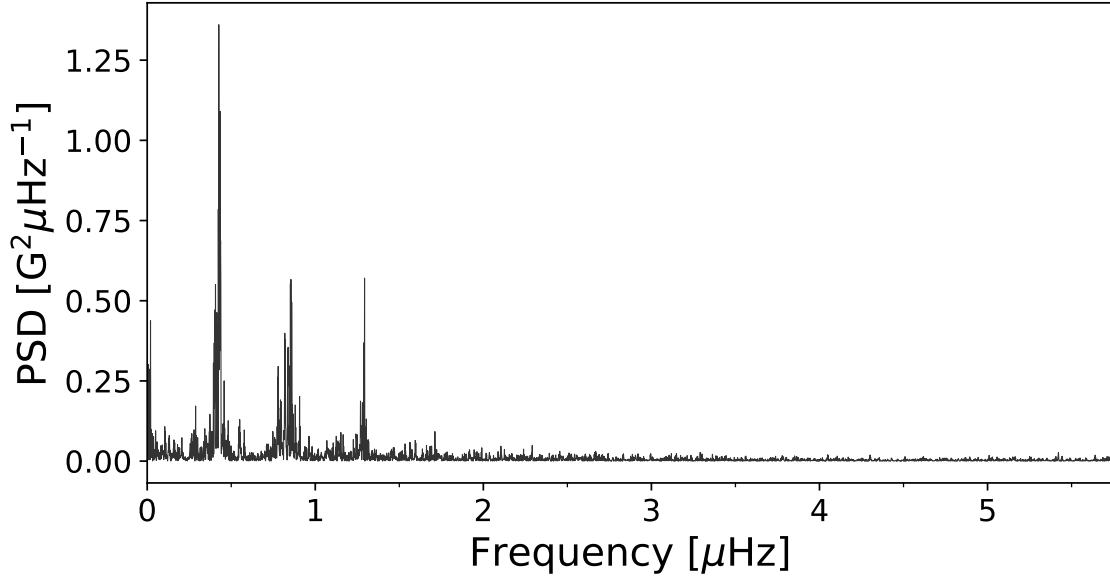
1.4.1 Identifying Features in the SMMF Power Spectrum

As we have 40-second cadence observations of the SMMF, we were able to investigate the power spectrum up to a Nyquist frequency of $12500 \mu\text{Hz}$. There are a number of features within the full power spectrum, shown in Figure 1.3.

The peaks between $0.1 - 2.0 \mu\text{Hz}$ are a manifestation of a persistent rotational signal in the SMMF. The distinct set of peaks indicates the existence of a long-lived, inhomogeneous, RM source. The SMMF signal exhibits a quasi-coherent



(a) BiSON SMMF 40-second cadence time series



(b) Power spectral density of the BiSON SMMF

Figure 1.2: (a) 40-second cadence observations of the SMMF from the Sutherland BiSON station between 1992 and 2012. The sense of the field was chosen to match the [Chaplin et al. \(2003\)](#) and the WSO observations, where positive is for a field pointing outwards from the Sun. (b) Power spectrum of the SMMF on a 40-second cadence truncated to $10\mu\text{Hz}$, however, the Nyquist frequency is $12500\mu\text{Hz}$.

behaviour in the time domain, and based on the comparatively short timescales for the emergence of magnetic features compared to their slow decay (i.e. hours–days compared to weeks–months) ([Zwaan, 1981](#); [Harvey & Zwaan, 1993](#); [Hathaway &](#)

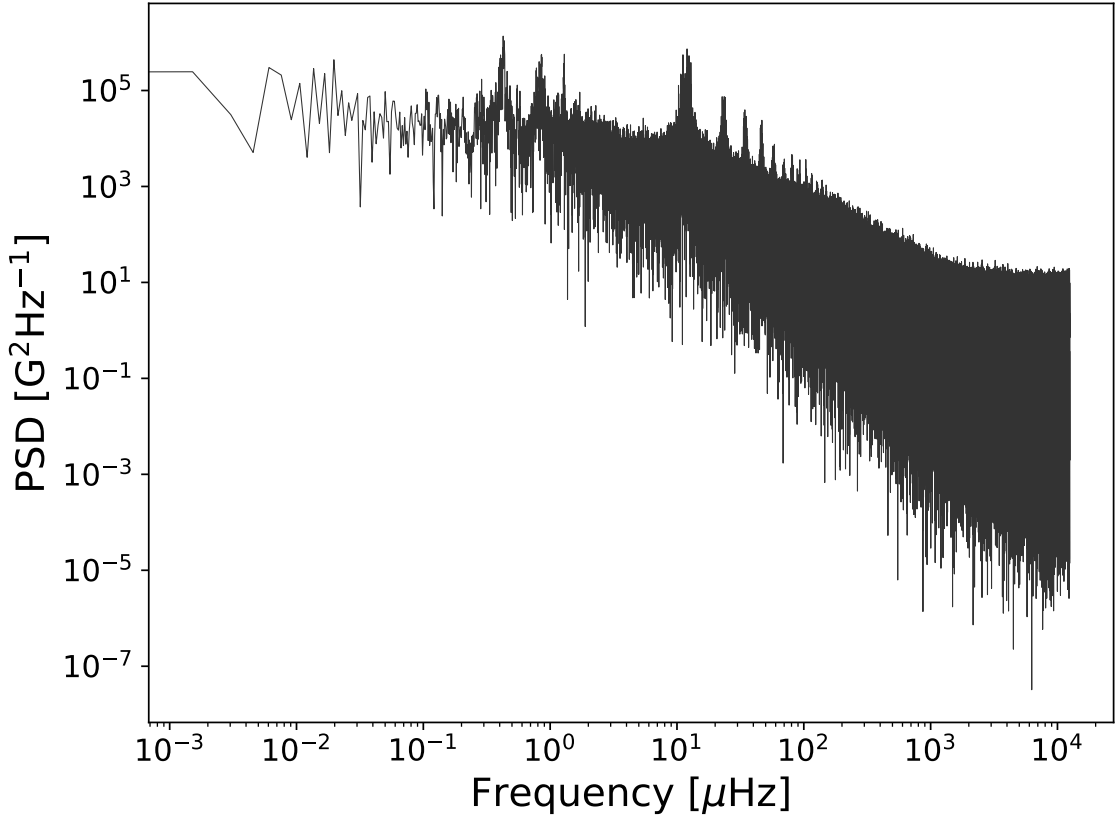


Figure 1.3: Power spectrum of 40-second cadence SMMF from the Sutherland BiSON station observed between 1992 – 2012 on a logarithmic scale up to the Nyquist frequency.

(Choudhary, 2008; Dacie et al., 2016), we assume the evolution of the RM component with time is a sudden appearance and a long, exponential decay.

The high Nyquist frequency was critical in uncovering a red-noise-like component in the power spectrum. This component could arise from continuously evolving, short-lived regions of magnetic field linked to magneto-convection, akin to a random walk, which we will dub the Stochastic Background (SB) component. Analogous to the SB, is the granulation signal observed in the Doppler-velocity measurements of the solar surface (Basu & Chaplin, 2017). It is indeed possible that this is not a real feature in the data and it could also be present due to the high-cadence and low-fill of the observations.

In addition, at low-frequency there is power associated with instrumental noise and solar activity, and at very-high frequency shot-noise is captured which sets the

lower limit in power in the spectrum.

There are also side-band features in the power spectrum at multiples of $1/\text{day} \sim 11.57 \mu\text{Hz}$. The side-bands are a well-known phenomena in ground-based helioseismology. They arise from gaps in the data which are a consequence of making single-site, ground-based observations of the Sun.

The duty cycle of the BiSON observations is very low, at around $\sim 15\%$, therefore it was important to take into consideration the effect that gaps in the data have on the power spectrum. Gaps in the data cause an aliasing of power from actual signal frequencies spread to other frequencies in the spectrum, and the nature of the aliasing depends on the properties of the window function of the observations. It is also possible that the SB component is an effect of power aliasing due to the low duty cycle of the data. Hence, before modelling the power spectrum, the window function was well-characterised.

Through understanding how the duty cycle of the observations affected the power spectrum informed the way we finally parametrised the full model of the power spectrum.

1.4.2 Parametrisation of the SMMF Power Spectrum

In the frequency domain, each of the RM peaks models well as a Lorentzian distribution, similar to peak-bagging modes of solar oscillations ([Handberg & Campante, 2011](#); [Davies et al., 2014](#)), which is due to the quasi-coherent nature of the source. The exponential decay of the RM SMMF source gives width to the peaks in the power spectrum, which we can measure to infer their lifetime.

A single, symmetric Lorentzian peak can be modelled by:

$$L_n(\nu; \Gamma, A_n, \nu_n) = \frac{2A_n^2}{\pi\Gamma} \left(1 + \left(\frac{\nu - \nu_n}{\Gamma/2} \right)^2 \right)^{-1}. \quad (1.10)$$

where ν is frequency, A_n is the Root Mean Square (RMS) amplitude of the RM component in the time-domain, Γ is the linewidth of the RM peak, ν_n is the frequency

of the RM peak, and n simply flags each peak. The mean-squared power in the time domain from the RM component of the SMMF is given by the sum of the A_n^2 of the individual harmonics in the power spectrum.

Upon closer inspection of the power spectrum it is possible to see that the peaks appear to exhibit an asymmetric shape (see Fig. 1.2 and Fig. ??). Taking inspiration from [Howe et al. \(2020\)](#), it is possible to allow for asymmetry, which is controlled by the asymmetry parameter, α , in equation (1.11) ([Stancik & Brauns, 2008](#)):

$$L_n(\nu; \Gamma, A_n, \nu_n) = \frac{2A_n^2}{\pi\Gamma(\nu)} (1 + (2X(\nu))^2)^{-1}, \quad (1.11)$$

where:

$$X(\nu) = (\nu - \nu_n)/\Gamma(\nu); \quad (1.12)$$

$$\Gamma(\nu) = 2\Gamma/[1 + \exp^{-\alpha(\nu - \nu_n)}]. \quad (1.13)$$

In the limit where $\alpha \rightarrow 0$, we see that $\Gamma(\nu) \rightarrow \Gamma$, thus the asymmetric expression equates to the symmetric expression.

The model function used to describe the RM signal in the power spectrum is given by equation (1.14); the sum of N Lorentzian-peaks:

$$P(\nu) = \sum_{n=1}^N L_n(\nu; \Gamma, A_n, \nu_n). \quad (1.14)$$

The subscript, n , describes a single peak in the power spectrum; in implementing the model we constrain the central frequency for each of the peaks such that they must be integer values of ν_0 : $\nu_n = n\nu_0$. This means that we define a single rotation frequency only, and subsequent peaks are harmonics. It is worth noting explicitly that this function assumes the linewidth of each Lorentzian peak is the same; only their amplitudes and central frequency differ.

When modelling the power spectrum we attempted the fit with both of the symmetric and asymmetric Lorentzian expressions, independently. Firstly we modelled

using the symmetric Lorentzian, and subsequently, using the asymmetric Lorentzian. This would determine whether there is a necessity for the addition of the asymmetry parameter.

Through both formulations we can measure the e -folding lifetime of the amplitude of the RM component (T_e), as it is related to the linewidth of the peak by equation (1.15):

$$\Gamma = (\pi T_e)^{-1}. \quad (1.15)$$

The low-frequency power due to instrumental drifts and solar activity can be incorporated into the model via the inclusion of a zero-frequency centred Lorentzian, i.e. Harvey-function, given by:

$$H(\nu; \sigma, \tau) = \frac{4\sigma^2\tau}{1 + (2\pi\nu\tau)^2}, \quad (1.16)$$

where σ is the characteristic amplitude of the low frequency signal, and τ describes the characteristic timescale of the excursions around zero in the time-domain.

Finally, the high frequency power is accounted for by the inclusion of a constant offset due to shot-noise, c .

1.4.3 Modelling the SMMF Power Spectrum

Parameter estimation was performed in a Bayesian manner using a Markov Chain Monte Carlo (MCMC) fitting routine. Following from Bayes theorem we can state that the posterior probability distribution, $p(\mathbf{a}|D, I)$, is proportional to the likelihood function, $L(D|\mathbf{a}, I)$, multiplied by a prior probability distribution, $p(\mathbf{a}|I)$:

$$p(\mathbf{a}|D, I) \propto L(D|\mathbf{a}, I) p(\mathbf{a}|I), \quad (1.17)$$

where D are the data, and I is any prior information.

To perform the MCMC integration over the parameter space we must define a

likelihood function; however, in practice, it is more convenient to work with logarithmic probabilities. The noise in the power spectrum is distributed as χ^2 2 degrees-of-freedom (Handberg & Campante, 2011; Davies et al., 2014), therefore the log likelihood function is:

$$\ln(L) = - \sum_i \left\{ \ln(M_i(\mathbf{a})) + \frac{O_i}{M_i(\mathbf{a})} \right\}, \quad (1.18)$$

for a model, M_i , with parameters, \mathbf{a} , and observed power, O_i , where i describes the frequency bin. This likelihood function assumes that all the frequency bins are statistically independent but the effect of the window function means that they are not. We handled this issue in the using simulations based on the artificial data discussed in Section 1.5.1.

The prior information on each of the parameters used during the MCMC is discussed below, in Section 1.5.2.

The affine-invariant MCMC sampler `emcee` (Foreman-Mackey et al., 2013) was employed to explore the posterior parameter space. The chains are not independent when using `emcee`, therefore convergence was interrogated using the integrated autocorrelation time. We computed the autocorrelation time and found $\tau \sim 120$ steps. Foreman-Mackey et al. (2013) suggests that chains of length $\geq 50\tau$ are often sufficient. After a burn in of 6000 steps, we used 7000 iterations on 50 chains to explore the posterior parameter space, which was sufficient to ensure we had convergence on the posterior probability distribution.

1.4.4 Comparison with the WSO SMMF

To provide comparative results on the inferences from the BiSON SMMF, we repeated the analysis on the power spectrum of the WSO SMMF. The WSO data are only provided on a daily cadence, hence the Nyquist frequency is lower than for 40-second BiSON data, at $\sim 5.79 \mu\text{Hz}$, and it was not possible to observe the SB component. The analysis was also repeated using the daily-averaged BiSON SMMF,

to provide a more direct comparison between BiSON and WSO.

The same parametrisation as outlined above was relevant to the modelling of the features in the WSO Power Spectral Density (PSD), and the RM peak were fit using a model with symmetric Lorentzian peaks and separately with asymmetric Lorentzian peaks.

1.5 Results

1.5.1 Investigation of the Window Function

Due to the low fill of data, we see the effects of daily and random gaps on the power spectrum. Periodic gaps in the data give rise to sidebands in the power spectrum and random gaps cause a more broadband shifting of power, meaning that some power from the low-frequency RM component in the power spectrum is aliased to higher frequencies. First we will concentrate specifically on the effect of daily, periodic gaps in the data. The daily, periodic gaps in the BiSON data, due to single-site observations, produce sidebands around a frequency of $1/\text{day} \sim 11.57 \mu\text{Hz}$ and its harmonics.

The frequency (and harmonics) of the RM component are located near zero ($\nu_0 \sim 0.4 \mu\text{Hz}$). We are usually only interested in the real, positive frequencies but due to their close proximity to zero, they are reflected back as a product of the aliasing and hence there are negative and positive side-bands in the complete power spectrum. When considering the aliased power, both the positive and negative side-bands must be taken into account. The aliased power is located at frequencies:

$$\nu_{n,i} = i \left(\frac{1}{\text{day}} \pm \nu_n \right). \quad (1.19)$$

where i denotes the side-band number, and n denotes the harmonic of the mode.

The side-band structure implied by equation (1.19) is shown clearly in the SMMF power spectrum in Figure 1.4. It is clear that we could therefore have used the

predicted locations of the aliased power and incorporated them into the model for the full power spectrum. This would, however, have required us to explicitly model some ~ 1100 groups of side-bands in order to cover this effect over the entire frequency range, and each group would have required a unique parameter to control the fraction of power that was contributed to the full PSD. It would have become computationally expensive to model each aliased peak and there would certainly have been room for degeneracy issues to occur.

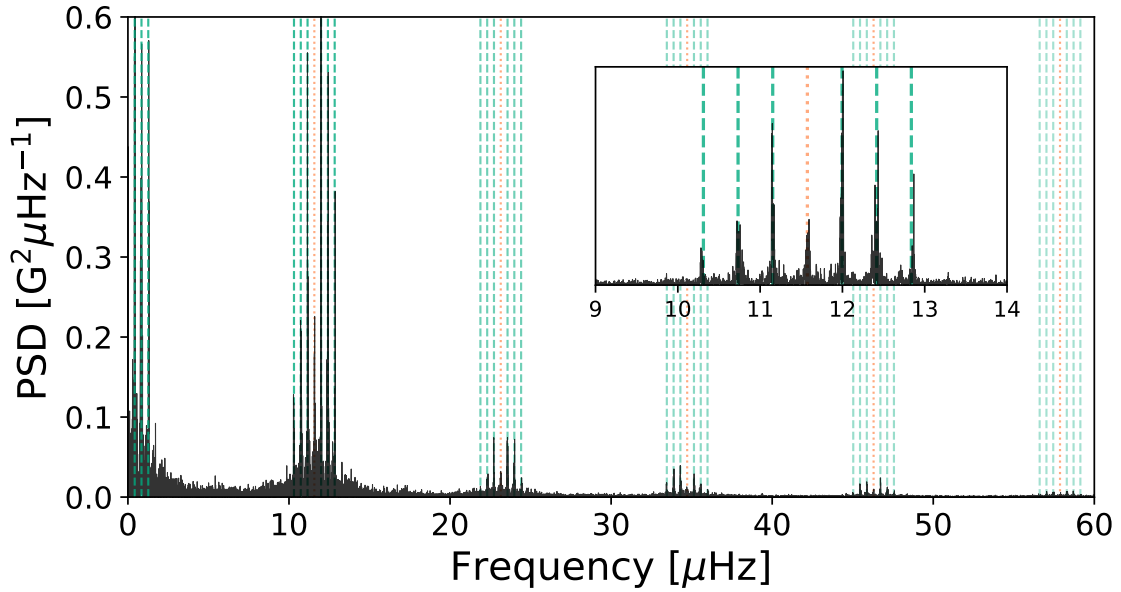


Figure 1.4: Locations of aliased power in side-band peaks. The orange, dotted-lines show the locations of frequencies at multiples of 1/day. The green, dashed-lines show the locations of the side-band peaks – harmonic frequencies reflected around multiples of 1/day. The inset shows a zoom of one set of side-band peaks around 1/day.

A more desirable, and we shall see more accurate, approach was to utilise the power spectrum of the window function itself. This approach not only takes into account the effect of daily, periodic gaps in the data, but also the more complex features that are added into the power spectrum due to the random gaps in the data. To do this, the Fourier transform of the window function describing the duty cycle of observations was computed (i.e. $|\mathcal{F}[g(t)]|^2$), where the duty cycle function, $g(t)$, is given by equation (1.20):

$$g(t) = \begin{cases} 1 & \text{for } |B(t)| > 0 \\ 0 & \text{for } |B(t)| = 0 \end{cases}. \quad (1.20)$$

In Figure 1.5 the power spectrum of the window function is shown. Furthermore, to demonstrate the effect of the window function on the power spectrum, an artificial spectrum was simulated with a single Lorentzian peak, following equation (1.14). By computing the inverse Fourier transform, an artificial time-series was generated over the same epoch as the BiSON SMMF observations. We were then able to examine the effects of injecting gaps into the data that were concurrent with the BiSON SMMF gaps.

As well as the power spectrum of the window function, Figure 1.5 also shows the underlying noise-free peak that describes the fake data and the power spectra of the artificial data with and without the injected gaps. The power spectrum of the BiSON SMMF data is also plotted for comparison.

It is strikingly clear from Figure 1.5 that the shape of the spectrum of the window function has a remarkable resemblance to the BiSON SMMF spectrum and the output of the artificial spectrum with gaps injected. This demonstrates that the periodic window function, with such a low duty cycle, has a dominating effect on the power spectrum of the input signal which not only produces the diurnal sidebands, but also a broadband spread of the power.

Due to the broadband shape of the window function power spectrum compared to the BiSON SMMF, it appears that there is actually no detectable red-noise-like, SB component in the SMMF; it is instead a manifestation of the periodic gaps in the data.

To analytically understand this effect, we can express the time series of observed data ($y(t)$) as a multiplication of the uninterrupted, underlying signal ($f(t)$) with the window function ($g(t)$), i.e.:

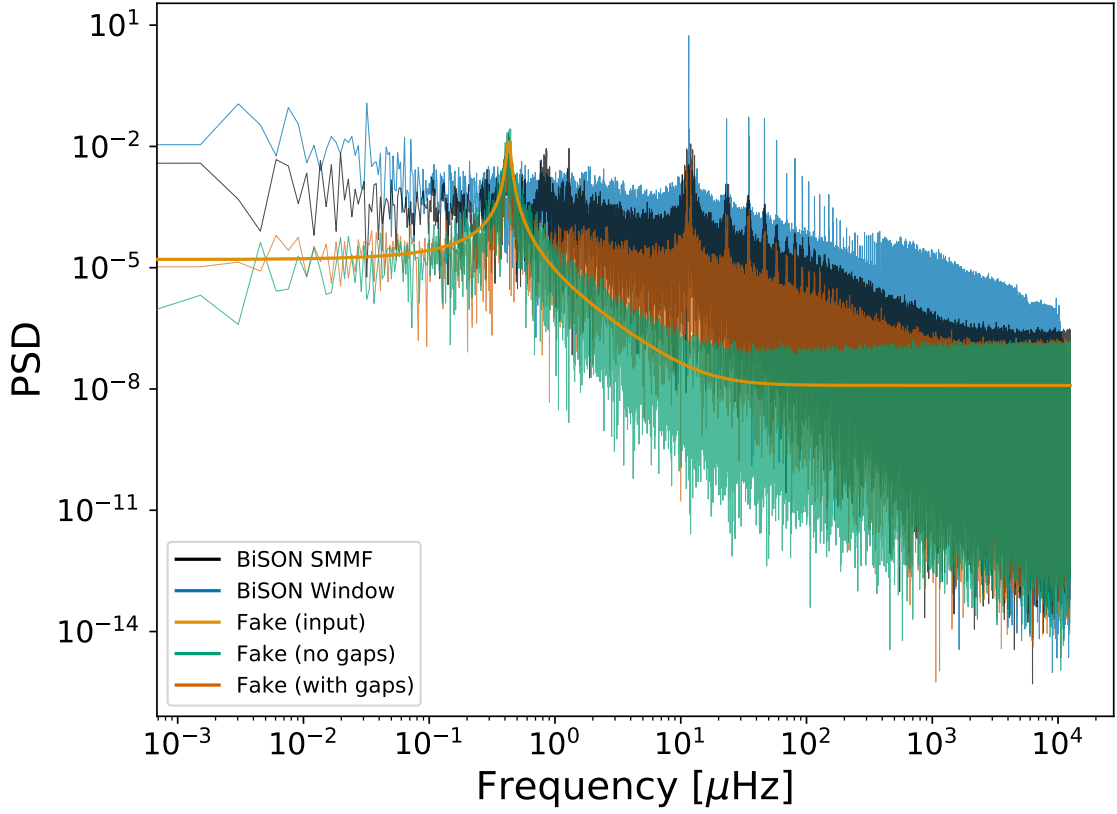


Figure 1.5: The effects of the window function on the power spectrum is shown by using a fake data set and this is compared to the BiSON power spectrum. Black line: BiSON SMMF PSD; blue line: power spectrum of the window function; green and dark-orange lines: the power spectrum of the artificial data without and with gaps, respectively; light orange line: the input peak used to generate the artificial data over-plotted. The power spectra of the BiSON SMMF and the window function have been shifted upwards by a factor of 6 and 30, respectively, for clarity.

$$y(t) = f(t) g(t). \quad (1.21)$$

In the frequency domain, as the Fourier transform of a product becomes the convolution of the transformed components. It is possible to express the observed power spectrum of data with periodic gaps in terms of the window function and the gap-free power spectrum, given in equation (1.22):

$$P'(\nu; \mathbf{a}) = P(\nu; \mathbf{a}) * |\mathcal{F}[g(t)]|^2. \quad (1.22)$$

Therefore to model the observed power spectrum in a robust manner, which takes

into account the intricacies caused by gaps in the data, we used a model which was formed of a model power spectrum, $P(\nu; \mathbf{a})$, convolved with the Fourier transform of the window function describing the duty cycle of observations ($|\mathcal{F}[g(t)]|^2$), i.e. a model described by equation (1.22), where:

$$P(\nu; \mathbf{a}) = \sum_{n=1}^N L_n(\nu; \Gamma, A_n, \nu_n) + H(\nu; \sigma, \tau) + c. \quad (1.23)$$

Care was taken to ensure Parseval's theorem was obeyed, and no power was lost or gained from the convolution operation:

$$\sum_{\nu} P'(\nu) = \sum_{\nu} P(\nu) = \frac{1}{N} \sum_t B(t)^2, \quad (1.24)$$

where N here is the number of observed cadences.

To demonstrate this method, as a proof-of-concept, we fit a model of a single Lorentzian peak, plus a shot-noise background, to the gap-free fake PSD (without the convolution) and the fake PSD using the gaps (requiring the convolution). The modelling was performed using the affine-invariant MCMC sampler `emcee` (Foreman-Mackey et al., 2013) to explore the posterior parameter space, and the results of this fit are summarised in Table 1.1.

Table 1.1: Model parameter values for the generation of artificial data, and the median posterior values for the fit to the power spectra generated with and without the gaps in the data. Numbers in brackets denote uncertainties on the last 2 digits, and all uncertainties correspond to the 68% credible intervals either side of the median.

Parameter	Input	Fit (no gaps)	Fit (gaps)	Unit
ν_0	0.42867	0.4277^{+18}_{-18}	0.4261^{+03}_{-03}	μHz
Γ	0.030	0.0279^{+37}_{-36}	0.0340^{+06}_{-06}	μHz
A	100.0	$101.2^{+7.3}_{-6.0}$	111.7 ± 0.1	mG
c	0.20	0.1872^{+03}_{-03}	0.1876^{+01}_{-01}	G^2Hz^{-1}

As we can see from the results in Table 1.1, the median values of the parameter posterior distributions without the gaps are in accordance with the input values, which were used when generating the artificial data, within uncertainties. When

the gaps were introduced, the median values of the parameter posterior distributions were close, but not within their uncertainties.

Through this demonstration we observed that, as a result of the convolution in the model, the widths of the posterior distributions for the model parameters were systematically underestimated. This effect arises because we do not account explicitly for the impact of the window function convolution on the covariance of the data. To perform the full likelihood evaluation, with the correlated noise, requires large-data computational linear algebra (i.e. the inversion of an N -by- N diagonal-constant/Toeplitz matrix, where N is the size of data); unfortunately the process of fully accounting for the correlated noise in this scenario was too computationally expensive, due to the large data set with $\sim 10^7$ data points. Our ability to resolve the model parameters is well represented in the case where the convolution was not performed; this helped us to understand how the convolution affected our ability to measure the true posterior widths, which allowed us to account for the systematic underestimate of the credible regions of the posterior distributions. We assumed the for ν_0 and c , we have an accuracy of $\sim 0.5\%$ each; for Γ , an accuracy of $\sim 15\%$; for A , an accuracy of $\sim 10\%$. Using these uncertainty estimates, the median values of the parameter posterior distributions for the convolution model are in accordance with the input values.

When modelling the power spectrum of the observed BiSON SMMF, these factors allowed us to account for the systematic underestimate of the posterior widths from the convolution.

1.5.2 Modelling the BiSON Power Spectrum

As there were many data points in the power spectrum, each likelihood calculation was computationally expensive. In order to reduce the required computation, the BiSON power spectrum was cut at a frequency of $7000 \mu\text{Hz}$, as at very high frequency, the spectrum purely represents the shot noise in the SMMF, and it was

deemed as a sufficient limit to still fully converge on the shot noise parameter.

The BiSON power spectrum was modelled against equation (1.22) (which used equation (1.23) with $N = 4$ peaks), for both the symmetric and asymmetric Lorentzian models, using the affine-invariant MCMC sampler `emcee` (Foreman-Mackey et al., 2013) to explore the posterior parameter space. In the modelling we used uniform prior information, providing reasonable boundaries on each parameter, as detailed below.

$$\begin{aligned}
\nu_0 &\sim \mathcal{U}(0.38, 0.50) \mu\text{Hz} \\
\Gamma &\sim \mathcal{U}(0.00, 0.11) \mu\text{Hz} \\
A_1 &\sim \mathcal{U}(100, 350) \text{ mG} \\
A_2 &\sim \mathcal{U}(50, 200) \text{ mG} \\
A_3 &\sim \mathcal{U}(20, 150) \text{ mG} \\
A_4 &\sim \mathcal{U}(10, 100) \text{ mG} \\
\sigma &\sim \mathcal{U}(0.01, 500) \text{ mG} \\
\tau &\sim \mathcal{U}(0.10, 200) 10^6 \text{ s} \\
c &\sim \mathcal{U}(10^{-3}, 10^2) \text{ G}^2 \text{ Hz}^{-1} \\
\alpha &\sim \mathcal{U}(-500, 0)
\end{aligned}$$

In Table 1.2 the median values of adjusted, marginalised posterior distributions for each of the model parameters are displayed, for both the symmetric and asymmetric models. The resultant posterior distributions were approximately normally distributed and there was no significant covariance between parameters, therefore uncertainties on the parameters correspond to the 68% credible intervals either side of the median. We note that we have previously shown the convolution results in a

systematic underestimate in the width of the posterior distributions and thus here we are presenting an estimation of the true uncertainties based on the factors acquired from the artificial simulations in Section 1.5.1.

Table 1.2: Median values of the marginalised posterior distributions for each model parameter in the fit to the BiSON power spectrum using symmetric and asymmetric Lorentzian profiles. Numbers in brackets denote uncertainties on the last 2 digits, and all uncertainties correspond to the 68% credible intervals either side of the median in the adjusted posteriors. The last row in the table shows the Bayesian Information Criterion (BIC) value for each model.

Parameter	40-s symm.	40-s asymm.	Unit
ν_0	$0.4270^{(+18)}_{(-18)}$	$0.4278^{(+18)}_{(-18)}$	μHz
Γ	$0.0264^{(+35)}_{(-35)}$	$0.0316^{(+41)}_{(-41)}$	μHz
A_1	166.0 ± 10.7	178.9 ± 11.5	mG
A_2	115.9 ± 7.4	129.0 ± 8.3	mG
A_3	83.2 ± 5.3	93.5 ± 6.0	mG
A_4	32.6 ± 2.1	38.9 ± 2.5	mG
τ	51.8 ± 6.8	62.7 ± 8.2	days
σ	83.4 ± 5.4	79.1 ± 5.1	mG
c	$0.2103^{(+03)}_{(-03)}$	$0.2102^{(+03)}_{(-03)}$	$\text{G}^2 \text{Hz}^{-1}$
α	–	-119.8 ± 15.7	–
<i>BIC</i>	<i>106</i>	<i>122</i>	–

As the asymmetry parameter converged reasonably within the prior bounds, we could deduce that the extra parameter was necessary; the model utilising asymmetric Lorentzian peaks was a better fit to the data than the model with symmetric Lorentzian peaks. However, we also calculated the Bayesian Information Criterion (BIC) to aid our model selection, to determine whether the asymmetry was truly necessary or a case of over-fitting to the data. The BIC for both the symmetric and asymmetric models were ~ 106 and ~ 122 , respectively. This highlighted that the model using the symmetric Lorentzian profiles was favoured, due to the lower BIC value.

The convolved model of the data, using symmetric Lorentzian peaks, is shown in Figure 1.6, over-plotted on top of the BiSON SMMF power spectrum.

The central frequency of this model, ν_0 , implies a synodic rotation period of 27.11 ± 0.11 days, and hence a sidereal rotation period of 25.23 ± 0.11 days. The

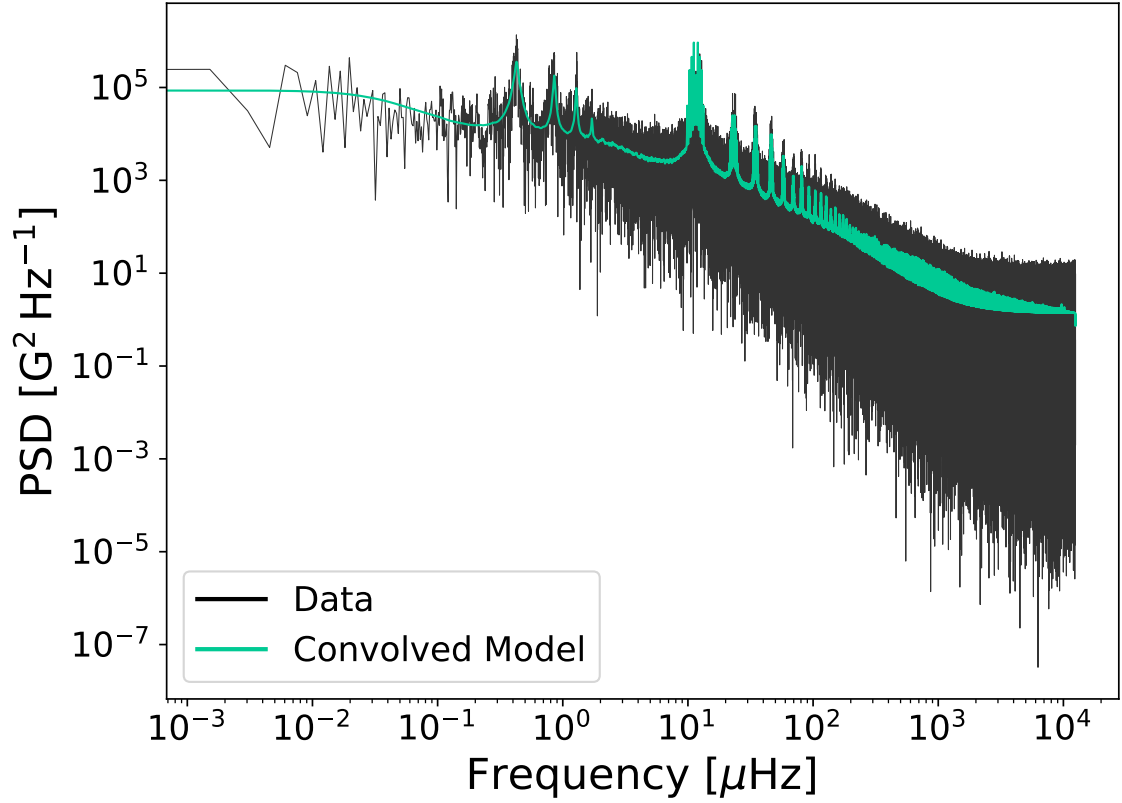


Figure 1.6: Full, modelled power spectrum of the BiSON SMMF on logarithmic axes. The data are displayed in black and the convolved model using symmetric Lorentzian peaks is shown in green.

rotation period measured is in agreement with other literature values for the rotation signal in the SMMF (Chaplin et al., 2003; Xie et al., 2017), and is in accordance with that typically observed for ARs and sunspots.

According to the model for differential rotation given by Snodgrass (1983) and Brown et al. (1989), the measured rotation period implies the RM component of the SMMF is sensitive to a time-averaged latitude of around 12° . This latitude is consistent with those spanned by sunspots and ARs over the solar activity cycle (Maunder, 1904; McIntosh et al., 2014), and particularly during the declining phase of the solar cycle (Thomas et al., 2019). This strongly implies that the origin of the RM component of the SMMF is linked to ARs and MFCs.

Furthermore, from the measured linewidth of the Lorentzian peaks, we have calculated the lifetime of the RM component using equation (1.15). The linewidth

suggests a lifetime of 139.6 ± 18.5 days, which is in the region of $\sim 20 \pm 3$ weeks. The typical lifetime of ARs and sunspots is usually on the order of weeks to months, dependent on their size (Zwaan, 1981; Schrijver & Harvey, 1994; Howard, 2001; Hathaway & Choudhary, 2008; van Driel-Gesztelyi & Green, 2015), therefore we have measured a lifetime of the RM component which is consistent with the lifetime of ARs and sunspots. This again suggests that the source of the signal is linked to active regions of magnetic field or similar MFCs.

Taking into account the work performed by Bose & Nagaraju (2018), which showed evidence to suggest sunspots did not contribute to the SMMF, and also our concerns with their methodology, we are cautious to specify that sunspots are the source of the RM component; however, this can still not be ruled out altogether. The method of identifying ARs or strong MFCs in magnetograms by Bose & Nagaraju (2018) potentially mis-identified regions of magnetic flux associated with ARs and MFCs as background flux and it is possible that they do contribute to the SMMF. By comparison with the work carried out by Kutsenko et al. (2017), the work performed in this project agrees that the SMMF is dominated by features with properties in-line with spots, ARs, and MFCs, i.e. long-lived and making up a small fraction of the solar disc, confined to active bands of latitude.

With all this considered, we state that our investigation of the BiSON SMMF indicates the SMMF has its origin in the vicinity of ARs and other concentrations of strong flux that are long-lived on the solar disc and exist in active latitudes. Whether or not specifically this is due to spots or other MFCs will require further work on the magnetogram thresholding techniques investigating the SMMF.

1.5.3 Comparison to the WSO Power Spectrum

Here we present the results from modelling the WSO power spectrum; we also show the results of modelling the power spectrum of the daily-averaged BiSON spectrum, to provide a direct comparison between both observations on the same cadence.

The fill of the WSO observations over the same epoch as BiSON observations was $\sim 78\%$, and at $\sim 55\%$ for the daily-averaged BiSON observations. As the fill of the daily-averaged BiSON data was higher than the 40-cadence data, the effect of the window function was less prominent. Nevertheless, the power spectra for both daily WSO and BiSON data were modelled using the convolution approach, as per the previous section. As, compared to the duty cycle of 40-cadence data, the fill is closer to 100%, we also expect the effect of the convolution to be less significant on the widths of the posterior distributions for each parameter, and thus the uncertainties to be more representative.

In addition, we also had to account for the sinc-function attenuation effect and reflections of power around the Nyquist frequency, due to the lower Nyquist frequency and its close proximity to the frequencies of the rotation peaks (Basu & Chaplin, 2017).

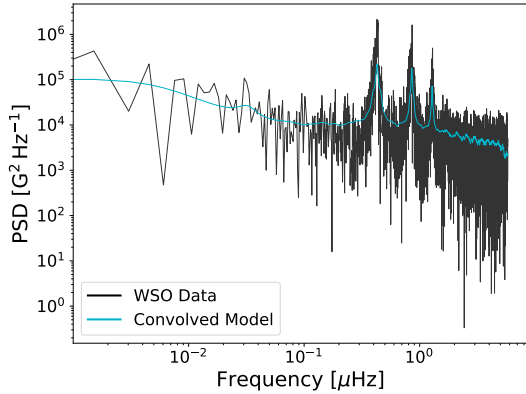
The daily-averaged BiSON power spectrum was modelled against equation (1.22) using equation (1.23) with $N = 4$ peaks, and similarly for the WSO power spectrum but with $N = 3$ peaks. Both fitting routines used the affine-invariant MCMC sampler `emcee` (Foreman-Mackey et al., 2013) to explore the posterior parameter space, using 10000 iterations on 50 chains. The convergence was again interrogated using the integrated autocorrelation time, to ensure a sufficient number of effective samples were used; hence ensuring that the posterior distribution was sampled.

In Table 1.3 the median values of marginalised posterior distributions for the model parameters are displayed, for both daily WSO and BiSON data. Reported uncertainties on the parameters correspond to the 68% credible intervals either side of the median. The systematic underestimate of the posterior width is much less of a concern with these results due to the higher duty cycle; the uncertainties are on the same order as the results not using a convolved model in Table 1.1. The convolved model for both the WSO and BiSON data, using symmetric Lorentzian peaks, are shown in Figure 1.7 over-plotted on top their respective SMMF power

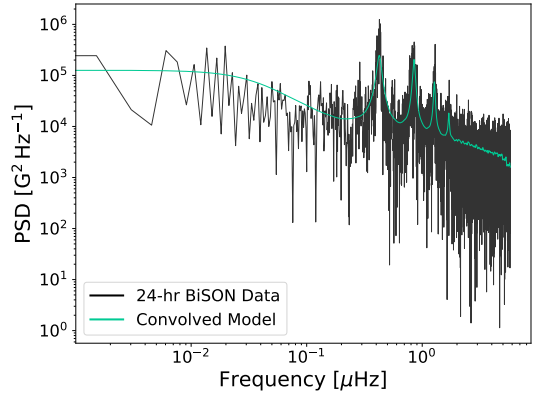
spectra.

Table 1.3: Median values of the marginalised posterior distributions for each model parameter in the fit to the daily WSO and BiSON power spectra. Numbers in brackets denote uncertainties on the last 2 digits, and all uncertainties correspond to the 68% credible intervals either side of the median. The last row in the table shows the BIC value for each model.

Parameter	WSO		BiSON 24-hr		Unit
	Symm.	Asymm.	Symm.	Asymm.	
ν_0	$0.4272^{(+05)}_{(-05)}$	$0.4290^{(+04)}_{(-04)}$	$0.4246^{(+08)}_{(-09)}$	$0.4270^{(+08)}_{(-08)}$	μHz
Γ	$0.0210^{(+16)}_{(-15)}$	$0.0210^{(+16)}_{(-15)}$	$0.0359^{(+27)}_{(-26)}$	$0.0365^{(+30)}_{(-29)}$	μHz
A_1	$134.8^{+3.1}_{-3.2}$	137.3 ± 3.5	$118.9^{+4.2}_{-3.8}$	$125.6^{+5.0}_{-4.4}$	mG
A_2	121.6 ± 3.4	$125.9^{+3.7}_{-3.6}$	$109.2^{+3.6}_{-3.8}$	$115.4^{+4.2}_{-4.4}$	mG
A_3	$75.1^{+3.5}_{-3.4}$	$78.9^{+4.0}_{-3.9}$	$64.6^{+3.7}_{-3.5}$	$70.1^{+4.2}_{-4.0}$	mG
A_4	—	—	$28.0^{+3.4}_{-3.3}$	$30.7^{+3.7}_{-3.6}$	mG
τ	$263.9^{+121.5}_{-83.3}$	$270.8^{+128.5}_{-84.5}$	$49.8^{+18.5}_{-12.7}$	$77.5^{+32.4}_{-22.0}$	days
σ	52.3 ± 4.6	$51.3^{+4.6}_{-4.5}$	$81.5^{+5.1}_{-1.1}$	$77.1^{+5.7}_{-5.5}$	mG
c	$11.7^{+18.7}_{-8.8}$	$11.0^{+18.4}_{-8.4}$	0.210 ± 0.011	0.210 ± 0.011	$\text{G}^2 \text{Hz}^{-1}$
α	—	$-61.7^{+13.3}_{-15.3}$	—	$-42.1^{+12.0}_{-15.1}$	—
BIC	47	55	55	63	—



(a) WSO



(b) 24-hr BiSON

Figure 1.7: Modelled power spectrum of (a) the WSO SMMF; (b) the daily-averaged BiSON SMMF, on logarithmic axes. The data are displayed in black and the convolved model using asymmetric Lorentzian peaks is shown in blue and green, for WSO and BiSON, respectively.

The results of the fit to the daily-averaged BiSON data are similar to those for the 40-second data, however there are a few differences which arise due to the different window functions and the realisations of the noise. We do however, generally, see

a good agreement between the parameters. We see in Figure 1.8 that there are differences between the daily averaged and 40-second spectra; at low frequencies it is possible to see the differences in the realisations of the noise, and at higher frequencies we can see differences due to the window function aliasing. This plot shows the possible reasons why the parameters in Table 1.3 may slightly differ from the results presented in Table 1.2.

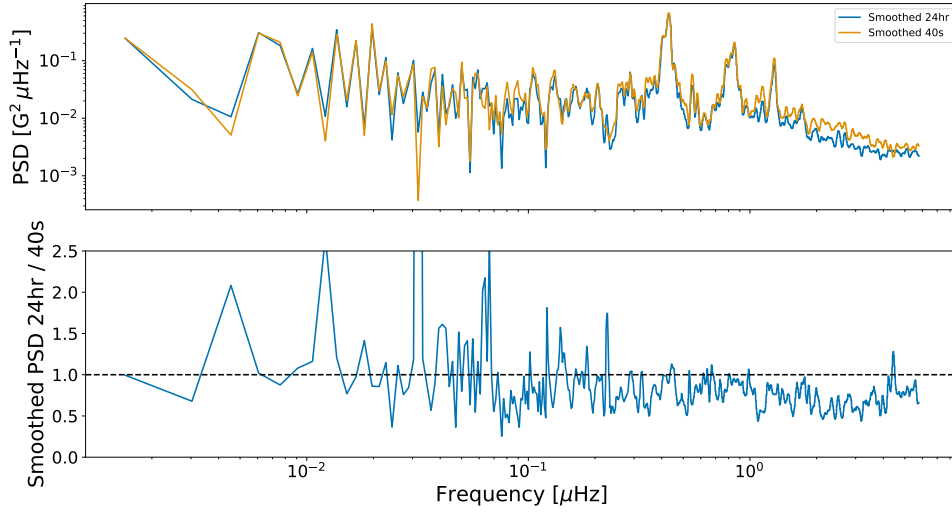


Figure 1.8: A comparison between the power spectra produced using the daily averaged BiSON data and the 40-second cadence BiSON observations. The top plot shows the log-smoothed power spectra of the daily averaged data (blue) and the 40-second data (orange). The bottom panel shows the ratio of the daily averaged data power spectrum to the 40-second data power spectrum. The horizontal, dashed line indicates a ratio of 1.

The fit to the WSO power spectrum using a model with asymmetric Lorentzian profiles converged on an asymmetry parameter, but as with the 40-second analysis of the BiSON data, we calculated the BIC values for both the symmetric and asymmetric model to determine which model to select. The BIC values for the WSO models using symmetric and asymmetric Lorentzian profiles were ~ 47 and ~ 55 , respectively, and the BIC values for the BiSON models using symmetric and asymmetric Lorentzian profiles were ~ 55 and ~ 63 , respectively. In both cases, this highlighted that the models using the symmetric Lorentzian profiles were favoured, due to the lower BIC values.

The rotation period in the WSO data is in agreement with that measured using

BiSON data to within 3σ , and this period implies a cycle-averaged latitude of around $\sim 12^\circ$. This agrees with the conclusions drawn from our inferences of the BiSON data, that the RM source is linked to ARs.

The linewidth from the WSO data suggests a RM lifetime of 175 ± 13 days, which is in the region of ~ 25 weeks or half a year. This lifetime is inconsistent with that measured using the daily averaged BiSON data, however. The lifetime measured in the BiSON power spectrum is around 50% larger than that measured with the WSO data. A possible explanation for this could be the resolution differences of the two instruments, or more likely it is a by-product of the different regions within the photosphere that each instrument probes. These limits are still consistent however with the lifetime of large, strong ARs (Schrijver & Harvey, 1994; van Driel-Gesztelyi & Green, 2015). The WSO lifetime is in agreement with the 40-second BiSON data, however.

As with the BiSON observations, the investigation of the WSO SMMF also indicates the origin of the SMMF is linked to ARs and MFCs that are long-lived on the solar disc and exist in active latitudes.

1.6 Discussion

1.6.1 Testing the Effects of Differential Rotation and Active Region Migration

We know the rotation period of ARs varies throughout the solar cycle as a result of solar differential rotation and latitudinal migration. As we have inferred that the RM component of the SMMF is likely linked to ARs and MFCs, we may therefore assume that the RM component is also sensitive to these effects. Here we analyse the effect of migration and differential rotation on our ability to make inferences on the lifetime of the RM component.

Several studies have modelled the the solar differential rotation, and its variation

with latitude and radius of the Sun (see [Beck, 2000](#); [Howe, 2009](#), for an in depth review of the literature on solar differential rotation). Magnetic features have been shown to be sensitive to rotation deeper than the photosphere; therefore, in general, magnetic features can be seen to rotate with a shorter period than the surface plasma ([Howe, 2009](#)).

[Chaplin et al. \(2008\)](#) analysed the effects of differential rotation on the shape of asteroseismic low- l p modes of oscillation, and showed that the consequence of differential rotation is to broaden the observed linewidth of a mode peak. The authors provide a model of the resultant profile of a p mode whose frequency is shifted in time to be a time-average of several instantaneous Lorentzian profiles with central frequency $\nu(t)$, given by equation (1.25):

$$\langle P(\nu) \rangle = \frac{1}{T} \int_0^T H \left(1 + \left(\frac{\nu - \nu(t)}{\Gamma/2} \right)^2 \right)^{-1} dt. \quad (1.25)$$

The angled brackets indicate an average over time. H and Γ are the mode height (maximum power spectral density) and linewidth, respectively. The full period of observation is given by T .

[Chaplin et al. \(2008\)](#) also show that by assuming a simple, linear variation of the unperturbed frequency, ν_0 , from the start to the end of the time-series by a total frequency shift $\Delta\nu$ (see equation (1.26)),

$$\nu(t) = \nu_0 + \Delta\nu \frac{t}{T}, \quad (1.26)$$

the resultant profile of a p mode can analytically be modelled by equation (1.27):

$$\langle P(\nu) \rangle = \frac{H}{2\epsilon} \arctan \left(\frac{2\epsilon}{1 - \epsilon^2 + X^2} \right), \quad (1.27)$$

where ϵ and X are defined in equation 1.28 and equation 1.29:

$$\epsilon = \frac{\Delta\nu}{\Gamma}; \quad (1.28)$$

$$X = \frac{\nu - [\nu_0 + (\Delta\nu/2)]}{\Gamma/2}. \quad (1.29)$$

As the mode linewidths are broadened by this effect, we evaluated whether our ability to resolve the true linewidth of the RM component, and hence its lifetime, was affected. To evaluate this we computed the broadened profiles given by both equation (1.25) and equation (1.27), and fit the model for a single Lorentzian peak, to determine whether the linewidth is recovered.

In the first instance, we computed the broadened peak using equation (1.25). Over the duration of the observations, we computed the daily instantaneous profile, $P(\nu(t))$. The time-averaged profile, $\langle P(\nu) \rangle$, is a weighted average of each instantaneous profile, where the weights are given by the squared, daily-averaged SMMF, in order to allow a larger broadening contribution at times when the SMMF amplitude is large.

In the second instance, we computed the broadened peak using equation (1.27). Over the duration of the observations the daily frequency shift is computed, $\Delta\nu$. The time-averaged shift, $\Delta\nu$, is a weighted average, where again the weightings are given by the squared, daily-averaged SMMF.

To determine the shift in the rotation rate with migration, we used the model of the solar differential rotation as traced by magnetic features (Ω_m) given by equation (1.30), where $\mu = \cos \theta$ and θ is the co-latitude ([Snodgrass, 1983](#); [Brown et al., 1989](#)):

$$\frac{\Omega_m}{2\pi} = 462 - 74\mu^2 - 53\mu^4 \text{ nHz}. \quad (1.30)$$

Finally, the time-dependence on the latitude of the active regions used the best-fitting quadratic model by [Li et al. \(2001\)](#).

In both instances, the broadened peak was modelled as a single Lorentzian peak using equation (1.10), with a width equivalent to that which was inferred from modelling the BiSON power spectrum. We use `emcee` ([Foreman-Mackey et al.,](#)

2013) to explore the posterior parameter space with priors similar to the fit to the full power spectrum.

Over the entire duration of the SMMF observations, the time-averaged profile was calculated, using equation (1.25), and this is shown in Fig. 1.9a. The broadened mode used the input parameters for the model using symmetric Lorentzians, outlined in Table 1.2, however, with the background parameter set to zero.

By eye, the broadened profile does not appear to have a significantly larger linewidth. The input linewidth was $0.0264 \pm 0.0035 \mu\text{Hz}$, and the fit to the time-averaged broadened peak produced a linewidth of $0.0262^{+0.0038}_{-0.0037} \mu\text{Hz}$. The linewidth of the broadened peak under this method was rather unchanged from that of the true peak, and both linewidths are within uncertainties of each other.

Table 1.4: Input linewidth and the median posterior values of the Lorentzian model each simulation. Numbers in brackets denote uncertainties on the last 2 digits, and all uncertainties correspond to the 68% credible intervals either side of the median.

Input Value	Weighted Fit	Analytic Fit	Unit
0.0264 ± 0.0035	$0.0262^{+0.0038}_{-0.0037}$	$0.0263^{+0.0038}_{-0.0037}$	μHz

The time-averaged frequency shift due to differential rotation was calculated, much in the same way as equation (1.25), to be $\Delta\nu = 0.01285 \mu\text{Hz}$. This shift was used to generate the broadened profile using equation (1.27). The broadened mode distribution also used the input parameters outlined in Table 1.2, however, with the background parameter set to zero.

Similar to the numerically broadened peak, by eye, the analytically broadened profile does not appear to have a significantly larger linewidth (see Fig. 1.9b). The input linewidth was $0.0264 \pm 0.0035 \mu\text{Hz}$, and the linewidth of the analytically broadened peak from the fit was $0.0263^{+0.0038}_{-0.0037} \mu\text{Hz}$, which was within the uncertainties of the linewidth of the input peak.

These results show that both numerically and analytically, the mode broadening effect of differential rotation and latitudinal migration does not affect our ability

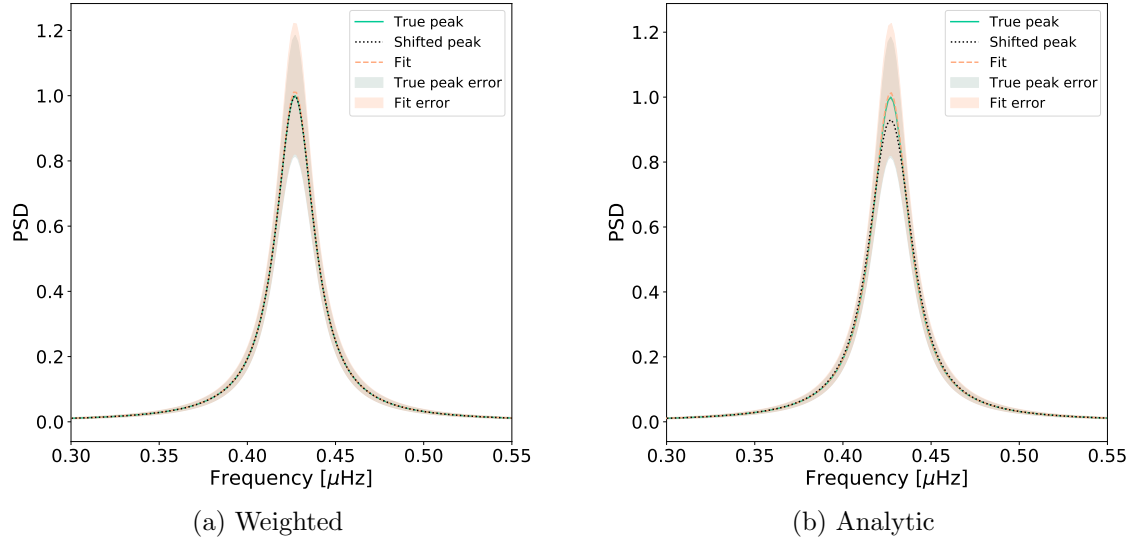


Figure 1.9: (a) Shows the Lorentzian distribution peak before and after the time-averaged broadening, and the fit to the broadened peak. (b) Shows the peak distribution before and after the analytical broadening, and the fit to the broadened peak. In both plots the broadened peaks have been shifted by the relevant frequency to overlay them on top of the true ν_0 for comparison.

to resolve the linewidth of the peaks. Both broadening methods applied have been shown to have a negligible effect on the measured linewidth. This result provides confidence that the linewidth in Table 1.2 is the true linewidth of the RM peaks, thus providing the correct lifetime for RM component, unaffected by migration and differential rotation.

1.6.2 Further Morphology of the SMMF using SDO/HMI Data

In Chapter 2 we acquired SDO/HMI full-disc magnetograms, using the `SunPy` python module (Barnes et al., 2020), to support our investigations into Rossby waves (see next chapter for details).

Owing to having the SDO/HMI magnetograms, which provided the capability to separately analyse the Northern and Southern Hemispheres' MMF contribution to the SMMF during the rising phase of Cycle 24 in 2011 and during solar maximum in 2014, we also investigated whether there were hemispheric differences in

the data, which resulted from the opposite polarities at high latitudes and towards the poles. This served as a further analysis into other timescales which may exist in the SMMF. In particular, we investigated whether the SMMF exhibited an anti-correlation between the two hemispheres due to the oppositely polarised field near the polar regions, as found in synoptic charts, on a time-scale of the solar cycle.

To support this investigation, we acquired the synoptic charts from SDO/HMI. It was possible to average the signal over the Northern and Southern Hemispheres of the synoptic charts, as well as the full solar surface, thus providing a comparison to the hemispheric MMF and the full disc SMMF.

To compare the magnetogram data to the synoptic charts, we smoothed the separately averaged Northern and Southern Hemispheres' MMF and the full-disc SMMF signals using a box-car filter with a window width of a Carrington period, i.e. ~ 27 days. The resultant time series was plotted along with the hemispheric mean of the synoptic charts from SDO/HMI. Figure 1.10 shows the resultant smoothed hemispheric MMF and full-disc SMMF along with the average of the synoptic charts.

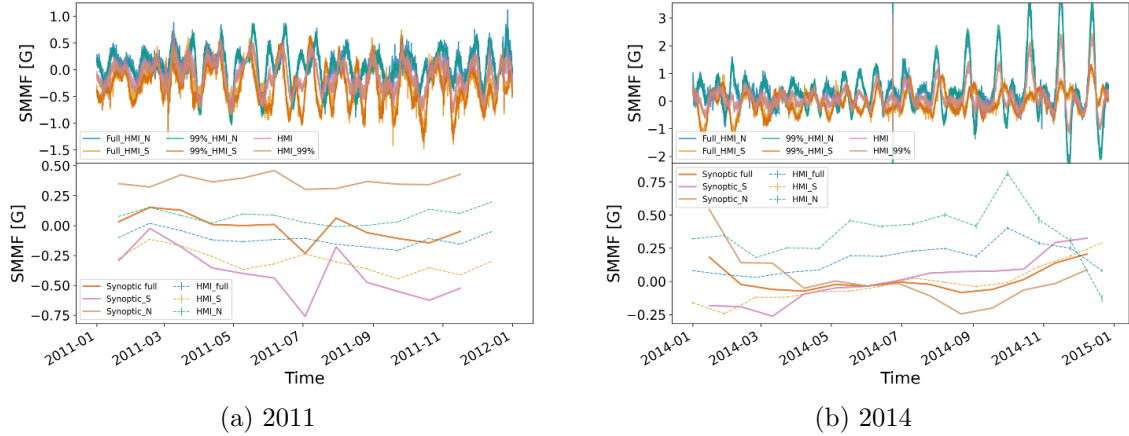


Figure 1.10: Investigations of timescales in the SDO/HMI magnetograms over 2011 and 2014. Both plots show in the top panel, the hemispheric MMF and full-disc SMMF from the magnetograms. The lower panel of each plot displays a comparison between the hemispheric and full-disc mean of the synoptic charts, compared to the box-car smoothed MMF from the magnetograms. N: Northern hemisphere; S: Southern hemisphere. Full HMI: considers the full solar disc; 99 HMI: considers only the inner 99% of the solar disc, by radius.

We can see from Figure 1.10 that there does exist a longer timescale in the hemi-

spheric MMF when we average out the effects of the RM component. This is visible from the reversal of the field polarity in 2014. This longer timescale component resembles the average of the synoptic charts, and shows the secular variation which is contributed by the solar dipole at high latitudes. This timescale is the solar activity period and can be seen particularly in Figure 1.10b. We see the beginning of a the magnetic field reversal at around solar maximum, in mid-2014, with the onset of the “rush to the poles” after solar maximum (Wilson, 1994; McIntosh et al., 2019).

Interestingly, the field reversal was located during different epochs when comparing the synoptic chart data to the visible disc, hemispheric MMF data, and was delayed in the hemispheric MMF by around 7 Carrington rotations.

Naturally, when the full-disc averaged SMMF was smoothed using the box-bar filter, the RM component was averaged out, resulting in a near-flat line. This was however expected as it was the average of the opposite hemispheres, and is consistent with the synoptic charts.

1.7 Conclusion

We have presented, for the first time, a frequency-domain analysis of over 20 years of high-cadence (40-second) BiSON observations of the SMMF.

Observations of the SMMF were computed from the Zeeman split D1 line of Potassium at ~ 770 nm, as measured by the Sutherland node of BiSON. The observations covered 7643 days over the period from 1992 – 2012 with a cadence of 40 seconds. A frequency-domain analysis of the SMMF was performed; the short cadence and long baseline of observations gave a fine frequency resolution in the power spectrum up to a high Nyquist frequency, allowing us to probe the elements that underpin the observed SMMF.

The duty cycle for the 40-second cadence observations was very low, hence the effect of the low fill on the power spectrum of the SMMF was investigated to help inform how to best model the full power spectrum. We highlighted that although

there appeared to exist a red-noise-like, stochastic background component in the power spectrum, this was a feature originating from power aliasing due to the low duty cycle of the observations.

In the power spectrum, there was a strong peak at a frequency corresponding to the solar rotation, denoted the RM signal/component. It was also demonstrated that the low duty cycle aliased the power of the prominent peak due to the solar rotation to higher frequencies, which provided several copies of this peak at higher frequencies.

Using a model comprising of a series of Lorentzian peaks to model the RM signal, a Harvey function to account for lower frequency drifts, and shot-noise limit, which was convolved with the Fourier transform of the window function to account for the low duty cycle artefacts, we modelled the full power spectrum and measured the properties of the RM signal.

It was demonstrated that the convolution process affected the total power in the model, thus careful treatment was taken to ensure Parseval’s theorem was obeyed. In addition, it was shown that the width of the posterior distributions for the parameters had been systematically underestimated, as a result of the convolution process, because we do not account explicitly for the impact of the window function convolution on the covariance of the data. We could not resolve this, but simulated data provided a comparison between a model with and without convolution which was used to provide a correction to account for the systematic underestimate of the credible regions of the posterior when modelling the power spectrum of the observed BiSON SMMF.

A comparative study was conducted on the WSO data over the same observational epoch and the modelled power spectrum provide results that were in agreement with those measured in the BiSON power spectrum.

To further investigate the SMMF and our ability to infer the properties of the source, we used simulations to analyse the effects of differential rotation and AR

migrations on our ability to measure the linewidth.

Finally, a short investigation into the SMMF as measured by SDO/HMI was conducted. Smoothing the data over the solar rotation period for both Northern and Southern hemispheres, separately, uncovered that the hemispheres display a longer variation, in accordance with the solar activity cycle, similar to that of the full-disc synoptic maps.

We leave the reader with the following points:

1. We have shown that there does not exist a short time-scale component in the SMMF, and the emergence of a red-noise-like signal in the power spectrum was due to the low duty cycle of the BiSON observations.
2. By modelling the peak of the RM signal as a symmetric Lorentzian profile, we found that the peak has a central frequency of $0.4270 \pm 0.0018 \mu\text{Hz}$. This measurement of the central frequency allowed us to infer the sidereal period of the RM signal to be 25.23 ± 0.11 days. This rotation suggests a magnetic feature, cycle-averaged latitude of $\sim 12^\circ$, thus linking the source to active bands of latitude on the Sun.
3. The lifetime of the source of the RM component was inferred from the linewidth of the Lorentzian peaks to be 139.6 ± 18.5 days, which is in the region of $\sim 20 \pm 3$ weeks.
4. As a comparison, the power spectrum of the SMMF measured by WSO was also modelled and the linewidth and central frequency of the RM component were measured. The results were generally consistent with those from the BiSON data, and the conclusions inferred were in accordance.
5. The measured properties of the RM component of the SMMF are consistent with ARs. The literature advises that sunspots are not the origin of the SMMF, here we suggest that ARs and MFCs are the source of the dominant,

rotation signal in the SMMF, that are long-lived on the solar disc and exist in active latitudes.

6. We have shown that our ability to determine the linewidth and hence lifetime of the RM modes was unaffected by AR migration and differential rotation.
7. Finally, a short investigation into the hemispheric contributions to the SMMF, using data from SDO/HMI, showed there is a longer-term variation which underpins the SMMF, in accordance with the activity cycle and polar field reversals.

At the time of writing, only two more of the BiSON nodes were actively measuring the SMMF (Las Campanas and Narrabri), and their measurements of the SMMF are not as stable as those measured by the Sutherland node. Sutherland has not been measuring the SMMF since 2013, however. More work is required to fix the issues with measuring the SMMF using BiSON, such that the frequency resolution can be further increased with a longer baseline, allowing for more accurate inferences on the SMMF morphology.

With more time on the project, it would also be useful to develop a technique similar to [Kutsenko et al. \(2017\)](#) and [Bose & Nagaraju \(2018\)](#), which allows the SMMF to be dissected into regions and features on the disc.

2 Rossby Modes in the Solar Mean Magnetic Field

2.1 Introduction

Rossby waves, as first derived by [Rossby & Collaborators \(1939\)](#), have recently been discovered in the Sun through observations of near-surface flows by the Solar Dynamics Observatory Helioseismic and Magnetic Imager (SDO/HMI) ([Löptien et al., 2018](#); [Liang et al., 2019](#)).

Standing Rossby waves, or r modes, are toroidal modes of oscillation of a rotating, fluid body for which the dominant restoring force against the pressure gradients is the Coriolis force ([Lanza et al., 2019](#); [Hathaway & Upton, 2020](#)). Rossby waves are associated with an undulation of a flow resulting in a pattern of radial vorticity of alternating sign. They are understood to form in the high atmosphere on Earth, heavily influencing global weather. For the Sun we observe that Rossby waves propagate in the retrograde direction, in the Carrington reference frame.

Recently, [Löptien et al. \(2018\)](#) provided an unambiguous detection of sectoral solar r modes by tracking the horizontal flows of granules in the solar photosphere during a 6-year period, using observations by SDO/HMI. Following this study [Liang et al. \(2019\)](#) confirmed the detection of solar r modes with time-distance helioseismology to measure deeper, subsurface flows in the meridional direction along the solar equator using both Solar and Heliospheric Observatory Michelson Doppler Im-

ager (SOHO/MDI) and SDO/HMI data, covering 21 years. In addition, [Hanasoge & Mandal \(2019\)](#) were also able to show the detection of solar r modes using a normal-mode coupling technique on 2 years of SDO/HMI data. In both of the observation conducted by [Löptien et al. \(2018\)](#) and [Liang et al. \(2019\)](#), the average lifetime of the r modes were on the order of several months, and as long as a over a year for specific modes.

By monitoring the proper motions of solar supergranules using a local correlation tracking method [Hathaway & Upton \(2020\)](#) also report observing low latitude Rossby waves in full-disc Doppler images obtained by SDO/HMI, extending the measurements of Rossby waves to greater depths in the solar atmosphere, by an order of magnitude. The r modes observed using the supergranules have lifetimes which are only slightly longer than the Carrington rotation period, hence in slight disagreement with [Löptien et al. \(2018\)](#) and [Liang et al. \(2019\)](#), which [Hathaway & Upton \(2020\)](#) claim may be due the waves getting in and out of phase with each other as the low wave number waves propagate faster than the higher wave number waves. As these observations are at low latitudes, it is possible that they are linked to active magnetic regions and hence could be manifested in other sources of magnetic data.

Here we present the search for evidence of a magnetic signature of the global r modes using over 20 years of Birmingham Solar Oscillations Network (BiSON) observations of the Line Of Sight (LOS) Solar Mean Magnetic Field (SMMF) (for details on the SMMF and BiSON, see [Chaplin et al. \(2003\)](#) and references within).

In Chapter 1, the power spectrum of the BiSON SMMF observations was modelled using a combination of Lorentzian peaks and a convolution with the window function to account for the effect of gaps in the data. The full spectrum and the fit are shown in Figure 2.1.

We can divide through by the model to achieve the residual spectrum, in which we have searched for the magnetic signatures of r modes. In this work the residual

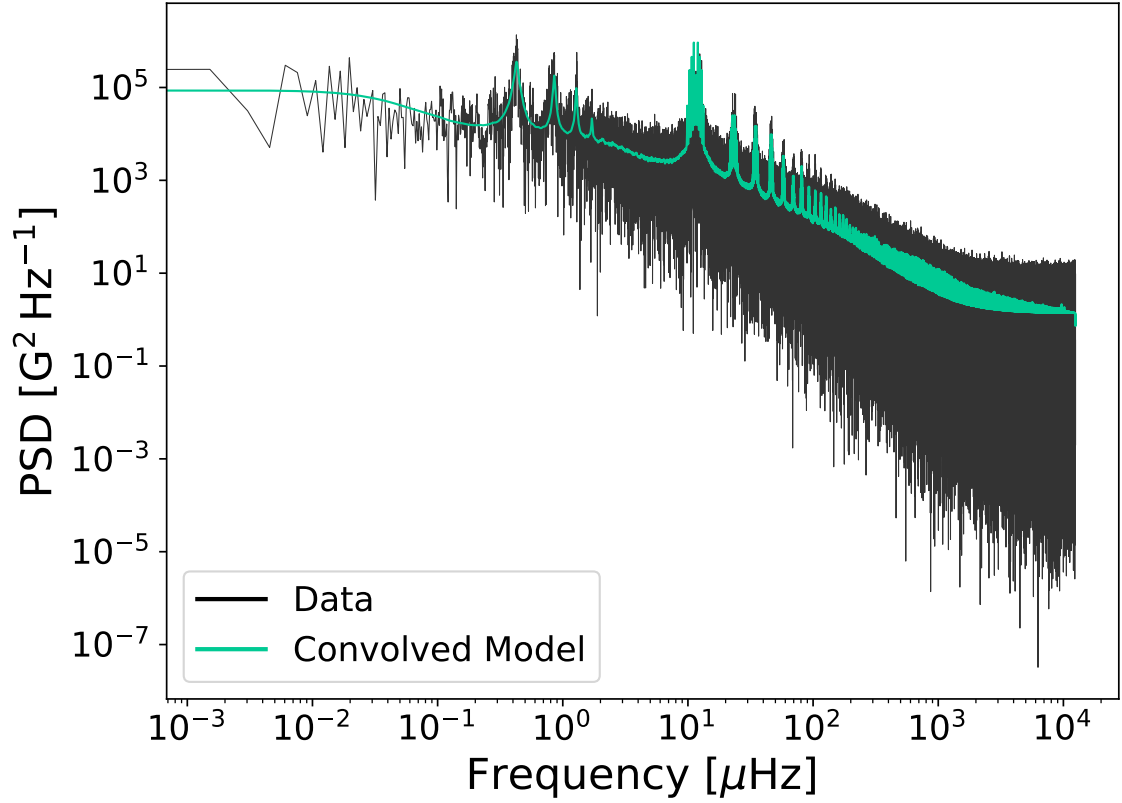


Figure 2.1: Full, modelled power spectrum of the BiSON SMMF on logarithmic axes. The data is displayed in black and the convolved model using symmetric Lorentzian peaks is shown in green.

spectrum was analysed to investigate the presence of r modes. Furthermore, analysis was performed using simulated data to better understand how an annual modulation of observations would affect any present r -mode frequencies.

2.2 Theory

The detailed theory of the effect of r modes on observational data was re-visited recently by [Lanza et al. \(2019\)](#) in light of the solar observations, in an effort to determine the effect of the r modes on radial velocity detections of exoplanets.

They showed that under the assumption of a slow, uniformly rotating sphere (with angular velocity, Ω , where $\Omega^2 \ll GMR^{-3}$), the frequencies of global r modes in the Carrington rotating frame is well approximated by:

$$\nu_{carr} = -\frac{2m\Omega}{l(l+1)}, \quad (2.1)$$

where $l > 0$ is the angular degree and m is the azimuthal order (Löptien et al., 2018; Lanza et al., 2019):

In an inertial frame the observed r mode frequencies will be (Lanza et al., 2019):

$$\nu_{in}(l, m) \approx m\Omega - \frac{2m\Omega}{l(l+1)} = m\Omega \left(1 - \frac{2}{l(l+1)}\right), \quad (2.2)$$

where Ω is the mean sidereal rotation rate, and l and m are the angular and azimuthal degree, respectively. Sectoral Rossby waves are obtained by setting $l = m$ in this equation. A consequence is that they propagate with a retrograde phase velocity as $\nu/m = -2\Omega/[m(m+1)] < 0$.

An Earth-based observer, orbiting the sun, shall expect to observe frequencies adjusted by the orbital frequency, $\nu_{\oplus} \approx 31.7\text{nHz}$, given by equation (2.3):

$$\nu_{obs}(l, m) = \nu_{in}(l, m) - m\nu_{\oplus}. \quad (2.3)$$

In addition, due to the tilt of the ecliptic with respect to the solar equatorial plane (the solar B_0 angle), the visibility of the modes will vary on a timescale of 1 year, meaning we expect to actually observe split peaks at frequencies of $\nu_{obs}(l, m) \pm \nu_{\oplus}$ (Lanza et al., 2019).

Based on this theory, we can predict the the frequencies at which to search for r modes. These frequencies are summarised in Table 2.1, along with the frequencies observed in other studies.

In Figure 2.2 we show the residuals spectrum with vertical lines indicating the locations of predicted r modes, based on Table 2.1. The solid lines indicate the location of the expected mode and the dashed lines show the expected locations of modes if split by the B_0 variation.

There appear to be resolved peaks in the vicinity of the $l = m = 2$ r mode and

Table 2.1: Predicted⁺ and observed^o r mode frequencies for combinations of l and m . Predicted frequencies and conversions of observations to different frames of reference use equation (2.1), equation (2.2), and equation (2.3), with $\Omega = 453.1$ nHz. The predicted splitting for the B_0 angle variation is also provided. The key for the source column is: LPT for Löptien et al. (2018), LNG for Liang et al. (2019), and LZA for Lanza et al. (2019).

Frequency	Source	$l = m = 2$	$l = m = 3$	$l = m = 4$	$l = m = 5$
$\nu_{carr} [nHz]$	LPT ^o	–	-259	-194	-157
	LNG ^o	–	-253	-198	-156
	LZA ⁺	-302.1	-226.6	-181.2	-151.0
$\nu_{in} [nHz]$	LPT	–	1100	1618	2109
	LNG	–	1106	1614	2110
	LZA	604.1	1132.8	1631.2	2114.5
$\nu_{obs} [nHz]$	LPT	–	1005.2	1491.7	1950.1
	LNG	–	1011.2	1487.7	1951.1
	LZA	540.8	1037.7	1504.4	1956.0
$\nu_{obs} + \nu_{\oplus} [nHz]$	LPT	–	1036.9	1523.3	1981.8
	LNG	–	1042.9	1519.3	1982.8
	LZA	572.4	1069.4	1536.1	1987.7
$\nu_{obs} - \nu_{\oplus} [nHz]$	LPT	–	973.6	1460.0	1918.4
	LNG	–	979.6	1456.0	1919.4
	LZA	509.1	1006.0	1472.7	1924.3

perhaps also the upper B_0 -variation-modulated $l = m = 3$ r mode. We therefore tested for the presence of these modes in the residual spectrum.

2.3 Methodology

2.3.1 Testing the Residual Spectrum

In order to investigate the presence of Rossby wave modes in the power spectrum of the BiSON SMMF, statistical significance tests were employed using a false-alarm approach, to test the probability of finding prominent narrow-band power in the residual spectrum.

We assume negative exponential statistics (i.e. χ^2 2-degrees of freedom distribution), and that the bins in the power spectrum are uncorrelated. This was tested using artificial data created with the same window function as the BiSON observations, and we showed that this assumption was suitable. We then calculated the

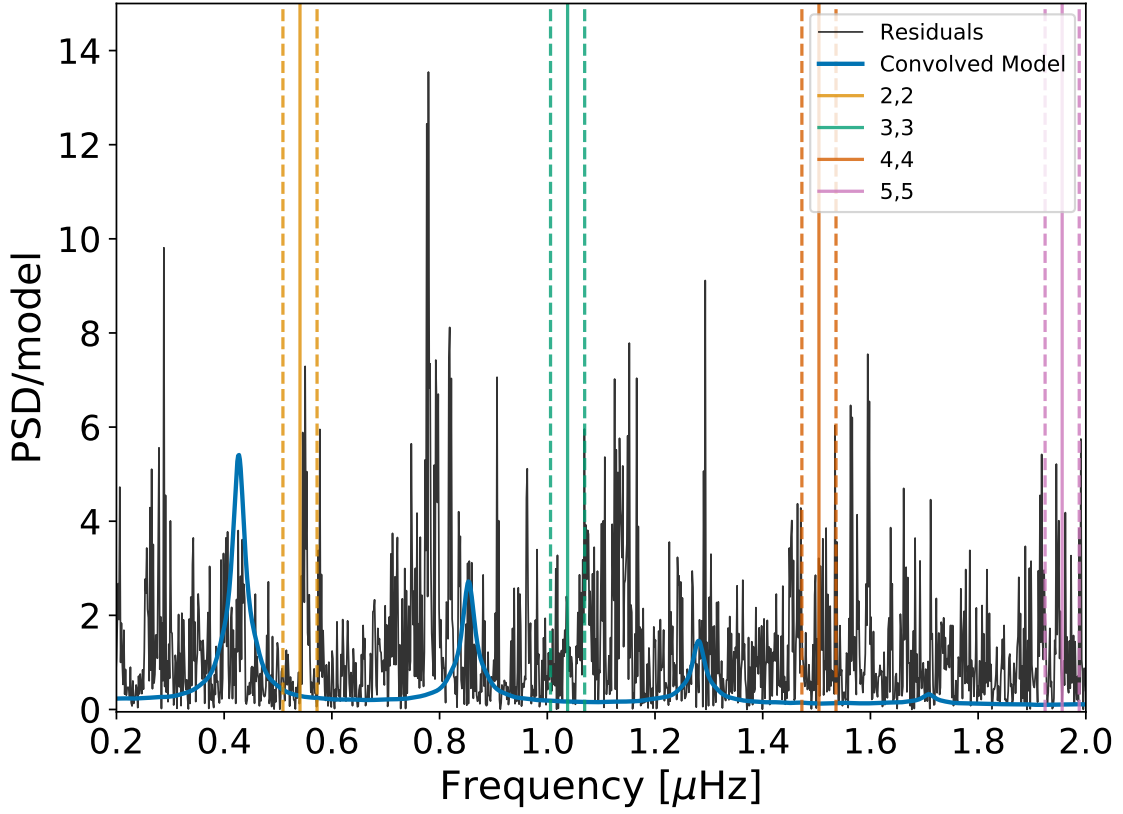


Figure 2.2: Residual power spectrum of the BiSON SMMF. Over plotted in the dark blue curve is the model of the main SMMF signal which was divided out from the raw spectrum. Also over plotted as vertical solid lines are the expected locations of the 4 lowest-frequency sectoral r modes and the dashed lines, the locations of the B_0 variation frequency splitting. Dashed lines represent ± 31.7 nHz (i.e. representing the frequencies of splitting due to the variation in the B_0 angle.)

false alarm probability, or probability to observe power in a given frequency bin, ν , that is greater than or equal to a given threshold. The probability to observe power in a given frequency bin, ν , that is greater than or equal to $P(\nu)$ is:

$$p[P(\nu)] = \frac{1}{P_{lim}(\nu)} \exp\left(-\frac{P(\nu)}{P_{lim}(\nu)}\right) \text{ or } p[P(\nu)] = \frac{1}{\langle P(\nu) \rangle} \exp\left(-\frac{P(\nu)}{\langle P(\nu) \rangle}\right), \quad (2.4)$$

where $P_{lim}(\nu)$ is the limit spectrum or $\langle P(\nu) \rangle$ is a well-fitting model/estimate to the spectrum. Considering a relative power approach (i.e. considering the power relative to the mean level or model of the Power Spectral Density (PSD)), equation (2.4)

may be written more concisely as:

$$p(s_\nu) = e^{(-s_\nu)} , \quad (2.5)$$

where,

$$s_\nu = P(\nu)/\langle P(\nu) \rangle , \quad (2.6)$$

and $\langle P(\nu) \rangle$ is reduced to 1 when we compare the power relative to the power spectrum residuals.

In reality, we used the χ^2 cumulative distribution function to compute the probability of power, which is given by equation (2.7), where k is the number of degrees of freedom, $\gamma(s, t)$ is the lower incomplete gamma function and $P(s, t)$ is the regularized gamma function:

$$F(x; k) = \frac{\gamma(\frac{k}{2}, \frac{x}{2})}{\Gamma(\frac{k}{2})} = P\left(\frac{k}{2}, \frac{x}{2}\right) . \quad (2.7)$$

Using these expressions, we can rewrite the equation for $P(s_\nu)$ as given by equation (2.8):

$$p(s_\nu) = 1 - F(2s_\nu; k) = 1 - P\left(\frac{k}{2}, s_\nu\right) . \quad (2.8)$$

This formulation provided the capability to compute the probability of statistically significant peaks in the residuals for re-binned data, for when data is binned over n -bins, the statistics becomes χ^2 with $2n$ degrees of freedom ([Appourchaux, 2004](#)).

The probability that a bin has power at or above the level s_ν is therefore given by equation (2.5), or more generally by equation (2.8), hence the probability that we fail to find a bin with power at or above the level s_ν is $1 - p(s_\nu)$; thus the probability of failing to find a bin with power at or above s_ν in N -bins in the spectrum is $[1 - p(s_\nu)]^N$. Therefore the probability to find at least one bin with power at or

above s_ν in N -bins in the spectrum is:

$$p_N = 1 - [1 - p(s_\nu)]^N, \quad (2.9)$$

where a low value for p_N indicates that the spike in power in that bin is unlikely to be a statistical fluctuation, and therefore is considered a statistically significant spike.

This can be generalised using the cumulative binomial distribution. The probability of finding at least r spikes in N -bins at or above the relative power level s_ν is given by equation (2.10), which is equal to equation (2.9) when $r = 1$,

$$p[r; p(s_\nu), N] = 1 - Pr(X < s_\nu) = \sum_{r=r}^N \binom{N}{r} p(s_\nu)^r [1 - p(s_\nu)]^{N-r}. \quad (2.10)$$

By applying equation (2.10) to the residuals of in the power spectrum, we can test whether there are any significant peaks in the residual power spectrum. Again, a low value for $p[r; p(s_\nu), N]$ indicates that the power in that bin is unlikely to be a statistical fluctuation.

2.3.2 Modelling r mode Profiles

In the location of any suspected r modes in the residual spectrum, we can model the profile of the peak by using a Lorentzian distribution using the form expressed by:

$$P(\nu) = \frac{2A^2/(\pi\Gamma)}{1 + (2(\nu - \nu_0)/\Gamma)^2}. \quad (2.11)$$

where A is the Root Mean Square (RMS) amplitude of the signal, Γ is the line-width of the distribution, and ν_0 is the central frequency of the distribution. This follows the methodology adopted by [Löptien et al. \(2018\)](#) and [Liang et al. \(2019\)](#). In practise, to ensure that we have parameters with dimensionality, this Lorentzian

distribution is fit co-added to the best-fitting model of the full power spectrum that was acquired in Chapter 1.

Parameter estimation was performed in a Bayesian manner using a Markov Chain Monte Carlo (MCMC) fitting routine. The likelihood function used was the χ^2 2 degrees-of-freedom (Handberg & Campante, 2011; Davies et al., 2014). The prior information on each of the parameters used during the MCMC is discussed below, in Section 2.4.

Modelling was performed using the pymc3 No U-Turn Sampler (NUTS) extension to a Hamiltonian Monte Carlo (HMC) sampling algorithm (Salvatier et al., 2016). Convergence was interrogated using the \hat{R} diagnostic factor using the criteria that chains did not converge if $\hat{R} > 1.01$.

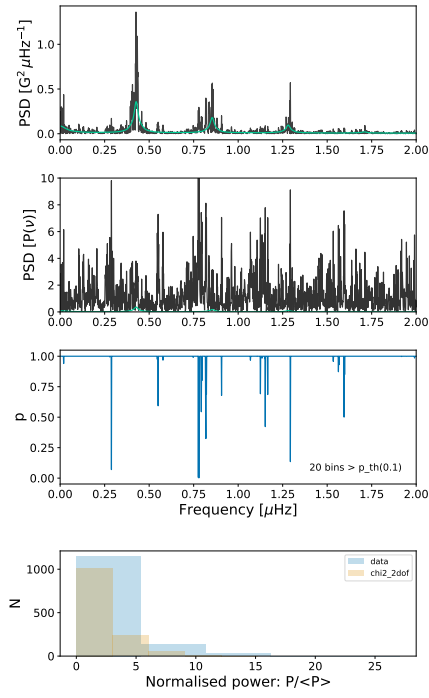
2.4 Results

2.4.1 Testing the Residual Spectrum

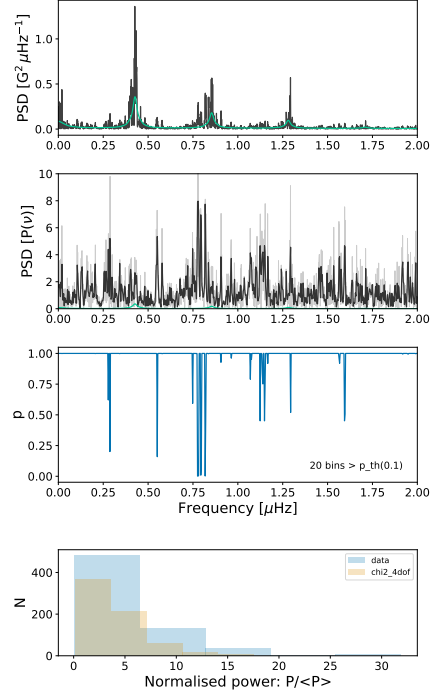
The residual spectrum was shown in Figure 2.2, highlighting locations of r mode frequencies predicted by Lanza et al. (2019). It is clear from Figure 2.2 that there appears to be a resolved peak of narrow-band power in both the location of the $l = m = 2$ r mode and perhaps also the upper B_0 -variation-modulated $l = m = 3$ r mode.

The statistics tests were performed on the residual spectrum for various re-binning factors, n . The plots summarising the statistics tests are shown in Fig. 2.3 for re-binning factors of $n = 1, 2, 5$, and 10 .

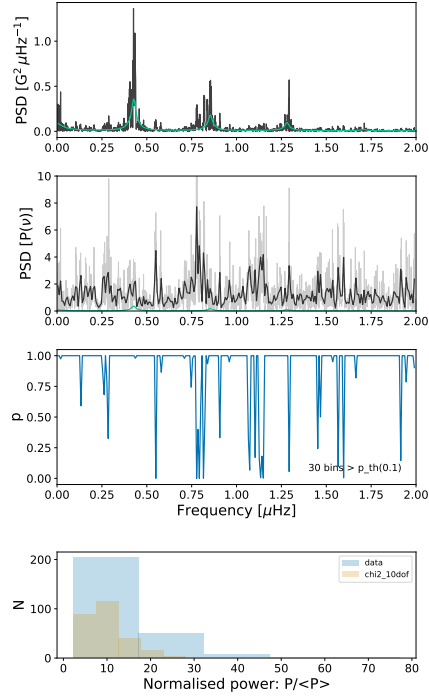
These tests suggest that the feature around $0.5 \mu\text{Hz}$ may be a signal related to r modes, as its location is roughly correct for the $l = m = 2$ mode consistently has a low False Alarm (FA) probability. In Figure 2.3b, there is compelling evidence to suggest that this feature is significant, in particular. In order to solidify this conjecture, we aimed to fit a model to the residuals around this peak in order to confirm whether the properties of the peak resembled those suggested by Löptien



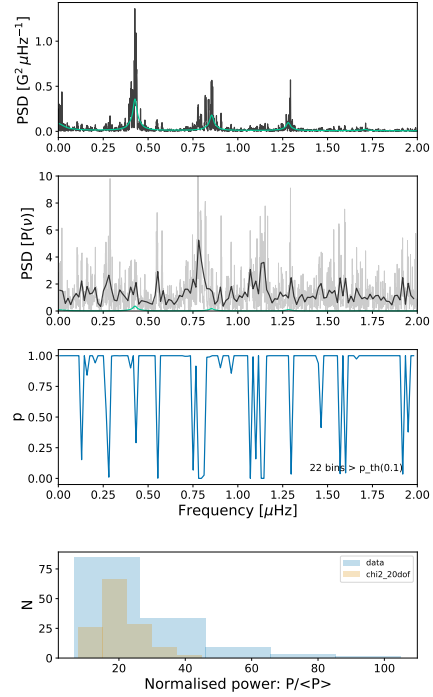
(a) No re-binning



(b) Re-binned by a factor of $n=2$



(c) Re-binned by a factor of $n=5$



(d) Re-binned by a factor of $n=10$

Figure 2.3: Realisations of the statistics tests on the BiSON data for different re-binning factors (n). The panels of each sub figure are: (top) the full PSD and fit, (second panel) the full and re-binned residuals, (third panel) the probability of statistical noise in each bin, (bottom) distribution of the residuals compared to a χ^2 $2n$ -DOF.

et al. (2018), Liang et al. (2019), and Lanza et al. (2019).

2.4.2 Modelling r mode Profiles

Using the model for the Lorentzian peak (eq. 2.11), with an additional parameter (c) for additional noise, we modelled the spectrum around the location of the potential $l = m = 2$ mode. The parameter space was sampled using `pymc3` and uniform priors were used, providing reasonable boundaries on each parameter, as detailed below.

$$\nu_0 \sim \mathcal{U}(0.54, 0.56) \mu\text{Hz}$$

$$\Gamma \sim \mathcal{U}(0.00, 0.05) \mu\text{Hz}$$

$$A \sim \mathcal{U}(0.0, 500.0) \text{ mG}$$

$$c \sim \mathcal{U}(-0.5, 0.5) \text{ G}^2 \text{ Hz}^{-1}$$

The results of the fit are given in Table 2.2 and the fit to the residuals is shown in Figure 2.4.

Table 2.2: Median posterior values of the Lorentzian model for the r mode peak in the BiSON SMMF PSD. Numbers in brackets denote uncertainties on the last 2 digits, and all uncertainties correspond to the 68% credible intervals either side of the median.

Parameter	Value	Unit
ν_0	$0.5500^{(+19)}_{(-19)}$	μHz
Γ	$0.0052^{(+49)}_{(-28)}$	μHz
A	$27.1^{+7.9}_{-5.9}$	mG
$bgnd$	$-0.002^{+0.059}_{-0.029}$	$\text{G}^2 \text{ Hz}^{-1}$

The median of the posterior distribution on the width parameter suggests an e-folding lifetime ($1/(\pi\Gamma)$) of around 710^{+670}_{-380} days ($\sim 1.9^{+1.8}_{-1.0}$ years), which follows the order of magnitude of the lifetime predicted and observed for low- m Rossby modes. The lowest r mode observed, $l = m = 3$, was shown to exhibit a lifetime of over a year (~ 1.4 years) by Liang et al. (2019). The $l = m = 4$ were observed by

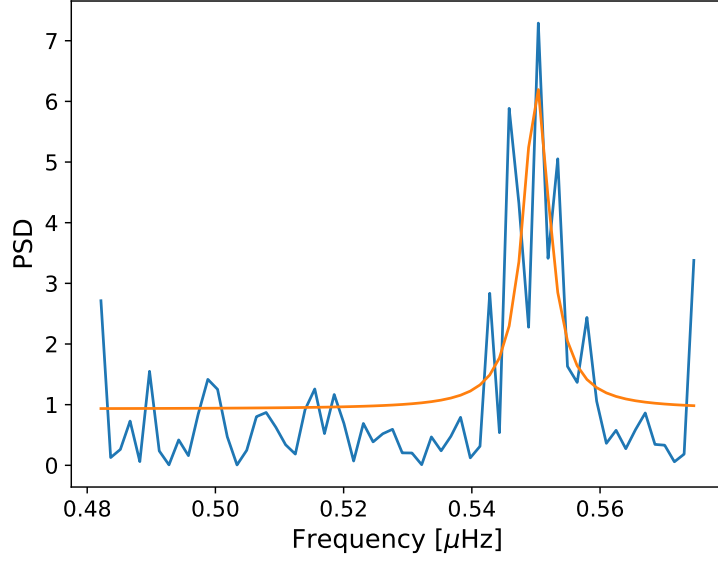


Figure 2.4: Model fit to the r mode in the BiSON PSD residuals using the median values from the posterior distributions of each parameter.

both [Löptien et al. \(2018\)](#) and [Liang et al. \(2019\)](#) to have a lifetime of ~ 0.6 years and ~ 0.3 years, respectively. There seems to be a slight increasing trend in the mode lifetimes observed by [Löptien et al. \(2018\)](#) and [Liang et al. \(2019\)](#) of longer lifetimes for lower m , therefore the long lifetime found here for the mode is entirely reasonable for the $l = m = 2$ mode and in-line with current observations.

The median value of the RMS amplitude of the peak was measured to be $\sim 27.1^{+7.9}_{-5.9}$ mG, which equates to a radial velocity amplitude of $\sim 7.8^{+2.3}_{-1.7}$ cm^{-1} . [Lanza et al. \(2019\)](#) state that the maximum RV amplitude of the $l = m = 2$ mode is $\sim 24.5 \text{ cm}^{-1}$, meaning our observed peak is around a third of the maximum RV amplitude one might have expected to observe. This is however an upper limit given by [Lanza et al. \(2019\)](#), and therefore the lower amplitude in the model should not be concerning.

In particular, however, we can see that the background is ~ 0 , which is expected. Due to the agreement between the central frequency of the fit to the $l = m = 2$ mode, the agreement in the order of magnitude of the e-folding lifetime, and the amplitude of the mode residing below the upper limit suggested by [Lanza et al. \(2019\)](#), there is evidence to suggest that this peak, which has shown to be significant

through the false-alarm statistics tests, could be the $l = m = 2$ sectoral r mode, observed in the BiSON SMMF data. We will cross-check this by further investigation using simulated data and, more directly, by comparison to other sources of SMMF observations, to determine whether the signal is present there too.

2.5 Discussion

Despite the results presented in the previous section there remained an open question on the way the Rossby waves would manifest themselves in the power spectrum. The BiSON power spectrum was also compared to the power spectra of the Wilcox Solar Observatory (WSO) SMMF and the SDO/HMI SMMF to cross-reference the finding.

2.5.1 Manifestation of Rossby Waves in the Power Spectrum

It was suggested by [Lanza et al. \(2019\)](#) that the mode should be split into two frequencies due to the annual variation of the B_0 angle, but the observed peak in the BiSON spectrum is located at approximately the location of the central frequency and is not split into significant peaks, separated by the predicted separation, due to this modulation. We needed to determine if this was physically observable.

Figure 2.5 shows a schematic diagram of the flow of a $l = 2 = m$ sectoral r mode. One can clearly see from the more visible purple region of the schematic, the Southern Hemisphere flow is oriented out of the page, whereas the Northern Hemisphere flow is oriented into the page. Due to the B_0 modulation, a varying of the sign of the flow would be observed over this region, i.e the velocity of the flow. In the more red-green regions the schematic, the flow is more transverse, hence this would contribute less to the effect of the B_0 modulation.

We needed to therefore understand whether the SMMF observations have a hemispheric dependence that would lead to a change sign in the observations due to the

B_0 variation. In addition, this raised the question of how the mode was affected in the power spectrum by the B_0 modulation; either split into separate peaks as suggested by [Lanza et al. \(2019\)](#) or instead was it possible that we could have a situation where the mode at the central frequency remained?

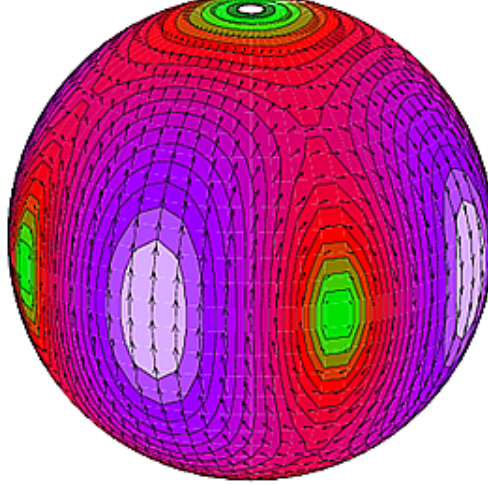


Figure 2.5: Mode displacement schematic for an $l = m = 2$ r mode ([Strohmayer & Mahmoodifar, 2014](#))

To investigate the splitting of the mode, a simple model was produced whereby a sinusoidal function (with a period of ~ 25 days) was modulated by either a cosine or rectified cosine function (with a period of 1 year). In the former, using the cosine modulation, this represents observing the sign of the flow varying with the B_0 modulation. Conversely in the latter simulation, this instead represents a variation of the amplitude, and it does not change the sign. It should be noted that the investigation of the mode splitting relies upon the assumption that the magnetic r mode signal has similar characteristics to the observed SMMF signal. Figure 2.6 shows the time series of the two cases to more clearly show their difference. The power spectrum of each case was then computed and these are shown in Figure 2.7 to demonstrate the differences between the modes produced.

One can clearly see the difference in the power spectrum produced in each of the cases. In the velocity modulation case, we see a splitting of the oscillation mode into two peaks split around the expected mode frequency by $\pm \nu_{\oplus}$. There exists no

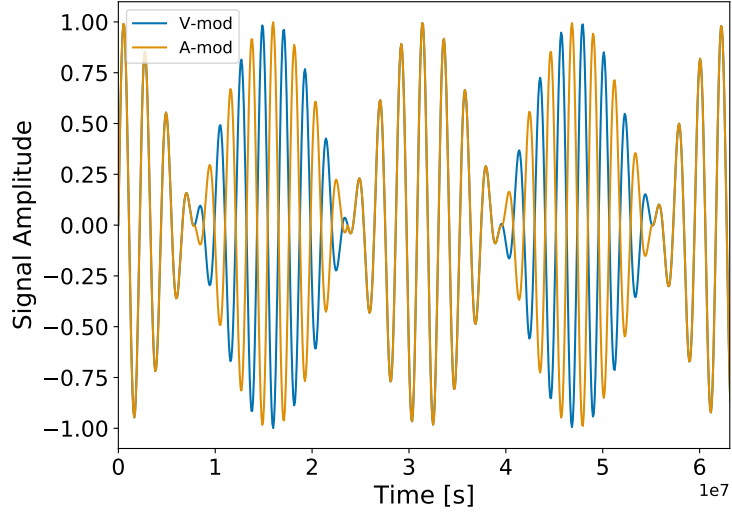


Figure 2.6: Time series of the velocity and amplitude modulation toy model simulations. The blue curve shows the velocity modulation, i.e. modulating using a cosine with period of 1 year, whereas the orange curve shows the amplitude modulation, i.e. modulating using a rectified cosine with period 1 year.

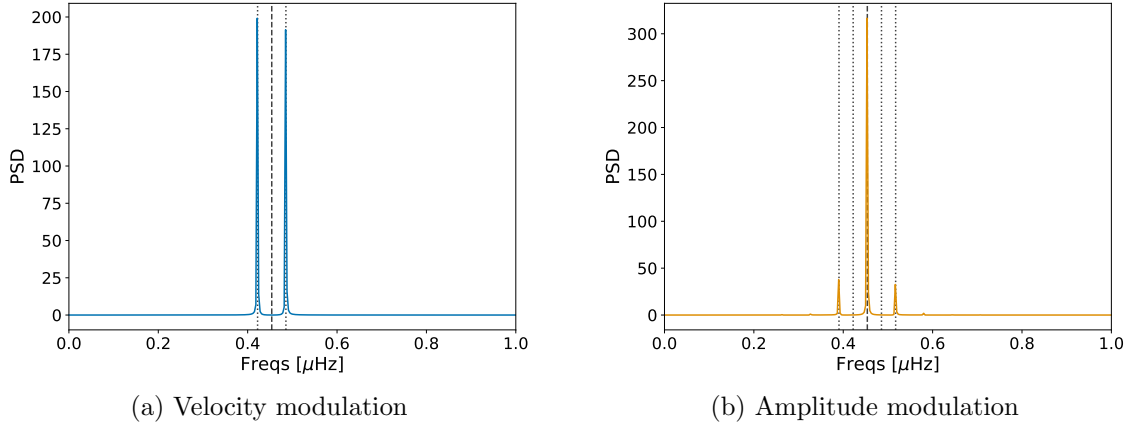


Figure 2.7: Power spectra for the two modulation methods, showing the difference in the way the modulation has changed the frequency of the observed mode.

more power at the central mode frequency in this case and is in agreement with the scenario suggested by [Lanza et al. \(2019\)](#). In the amplitude modulation case, we see sidebands at $\pm 2\nu_{\oplus}$ however the expected mode frequency remains in this scenario and has a significantly higher peak height, a ratio of 90:10 in favour of the central peak.

We have shown that it is possible to retain the central frequency of the r mode in the power spectrum if the B_0 modulates the amplitude of the observations and

not the sign. With this known, it was then necessary to understand whether the two hemispheres of the Sun contribute signals that are more analogous with the velocity modulation or amplitude modulation. In the former, velocity modulation, we would expect to see a persistent anti-correlation between the two hemispheres. In the latter, amplitude modulation, we would expect to see the signals from each hemisphere that are correlated, which track each other and which can be both positive or negative.

We investigated how the two hemispheres of the Sun contribute to the SMMF through analysis of SDO/HMI data. To do this, we acquired 720s-cadence magnetograms from SDO/HMI using the `SunPy` python module (Barnes et al., 2020) for the rising phase of solar cycle 24 during 2011, and for the maximum of cycle 24 during 2014. It was possible to separately average the Northern and Southern Hemispheres' contributions to the total, disc-averaged SMMF. The plot of this data is shown in Figure 2.8.

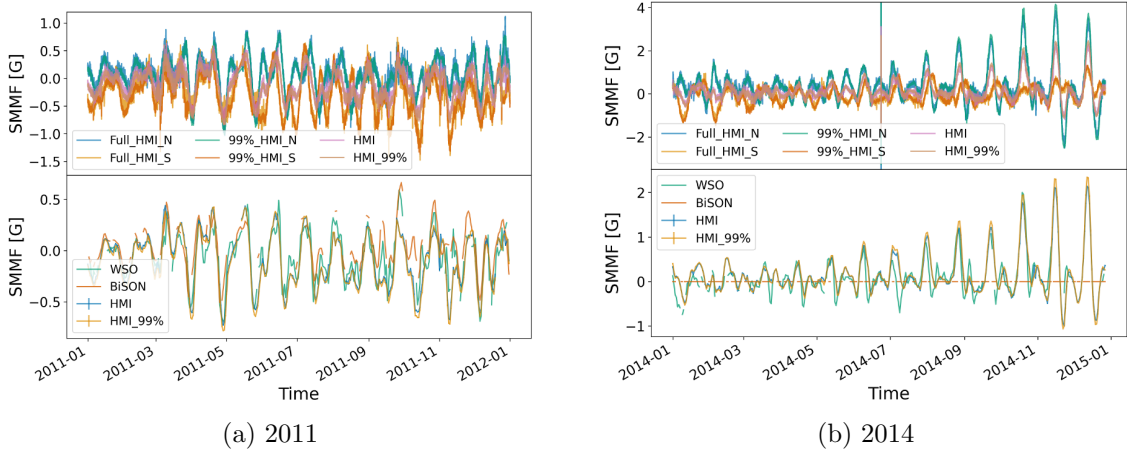


Figure 2.8: SDO/HMI SMMF split into hemispheres and compared to other SMMF sources during (a) 2011, and (b) 2014. The top panel in each figure shows the north (N), south (S), and total disc-averaged mean magnetic field, for both the full solar disc and from pixels within 99% of solar radius. The bottom panels show a comparison between the SMMF, as observed BiSON, WSO, and SDO/HMI (full disc and the 99% disc).

The hemispheric contributions to the total, disc-averaged, SMMF can be seen in Figure 2.8 to track each other during 2011, and both become positive or negative.

By contrast, when observing the hemispheric contributions to the full SMMF in 2014, we see that there are frequent periods of strong anti-correlation between the Northern and Southern Hemispheres. There are also several periods in 2014 whereby the two hemispheres are correlated. This plot aids in our understanding of how the r modes would be manifested in the power spectrum due to the variation of the B_0 angle.

As there are periods of both strong correlation and strong anti-correlation between the two hemispheres, this is a good indication that the r mode signal would result in a central frequency with sidebands due to the correlation between North and South. But due to the existence of periods of anti-correlation between North and South, we also expect there to be some degree of frequency splitting in the power spectrum, but this is dependent on how prevalent the anti-correlation is over the entire solar cycle; in these short epochs however, we expect this to be minimal. It is therefore possible to conclude that we are confident we are observing the $l = 2 = m$ r mode.

As a further point, we see that there is both strong correlation and strong anti-correlation between the Northern and Southern Hemispheres, however this does not necessarily mean that the r mode signal would directly manifest itself in the same way. We can see from Figure 2.5 that if the r mode observations are constrained to active latitude bands, closer to the equator, then the effects of the B_0 are less prominent.

2.5.2 Rossby Modes in Other Sources of SMMF Data

To further investigate whether the observation of the $l = 2 = m$ r mode is real, a comparison was made between the power spectrum of the BiSON observations of the SMMF and those from WSO and SDO/HMI, to determine whether the suspected r mode is visible. In the case of the WSO, the power spectrum was computed over the same observing epoch as the BiSON data (i.e. from 1992 – 2012); however SDO

was not launched until 2010, so for HMI the power spectrum was computed on data from 2010 – 2020, hence at approximately half the frequency resolution of WSO and BiSON.

Figure 2.9 shows the comparison of the WSO and SDO/HMI power spectra reflected around the x-axis against the BiSON power spectrum. In both cases we see a good agreement between the different sets of data on the location of the rotational mode in the SMMF, but there does not appear to be a visible r mode candidate in the WSO or the SDO/HMI data.

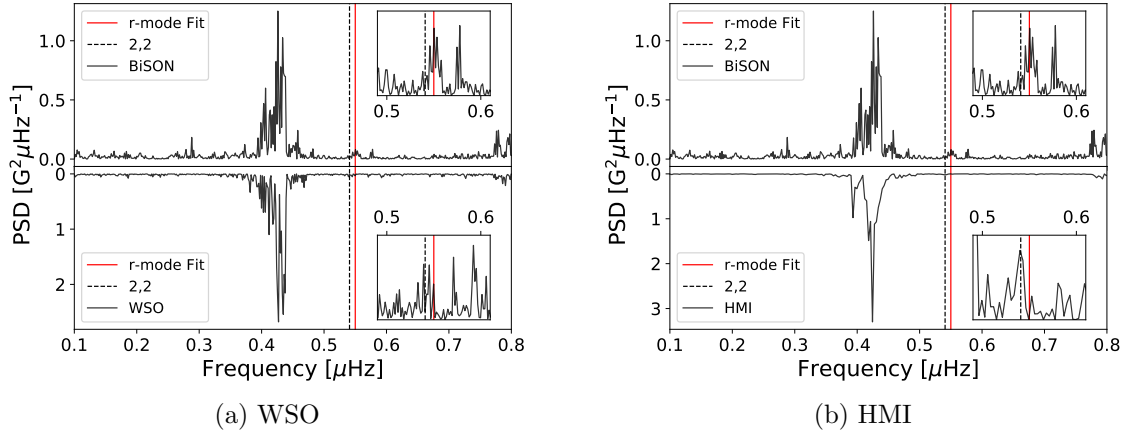


Figure 2.9: Comparison of the power spectra for BiSON, WSO, and SDO/HMI. In both figures, the top panel shows the BiSON PSD and the bottom panel shows either the WSO or HMI PSD. The dashed, black line shows the location of the theoretical $l = 2 = m$ r mode frequency, and the red, solid line shows the location of the peak fit in the BiSON PSD residuals.

This provides concerning evidence that we may not, in fact, have observed the $l = 2 = m$ r mode in the BiSON power spectrum, and perhaps instead we have a persistent noise source in the BiSON SMMF.

However compelling the results are, suggesting that we may have observed the $l = 2 = m$ r mode in the BiSON power spectrum, it is impossible to ignore that it is not present in two other sources of SMMF observations – of which one of these telescopes is responsible for providing the recent observations of r modes documented in the literature (SDO/HMI). Owing to this, we cannot conclude that we have observed the $l = 2 = m$ r mode in the BiSON power spectrum. We recommend

that searching for r modes in the power spectra of the SMMF observations should be revisited in a few years, or say a solar cycle's time, when the frequency resolution in each power spectrum has increased significantly, to provide a more insightful follow-up study.

2.6 Conclusion

After removing the model for the BiSON SMMF power spectrum we investigated the residual spectrum to search for evidence of a magnetic signature of global Rossby modes (r modes). A statistically significant peak was identified near the $l = 2 = m$ r mode frequency calculated by [Lanza et al. \(2019\)](#), which was further modelled to examine whether it was the r mode.

Using a model for the peak, following the description of r mode given by [Löptien et al. \(2018\)](#) and [Liang et al. \(2019\)](#), we identified the properties of the peak and compared it to the expected values in the literature.

To further interrogate the inferences on the statistically significant peak in the BiSON SMMF power spectrum, we used simple simulations to determine how the r mode may manifest itself in the power spectrum, and SDO/HMI hemispheric data were examined as a cross-reference.

As a final check, we compared the power spectrum of the SMMF observations from BiSON to those from WSO and SDO/HMI. There were no statistically significant peaks in the vicinity of the $l = 2 = m$ r mode in either of the other power spectra. Because this peak was only observed in one of three data sets, and particularly not in the SDO/HMI data which recent observations of sectoral Rossby waves in the Sun have all used, we could not conclude that the statistically significant peak in the BiSON SMMF was the $l = 2 = m$ r mode.

We leave the reader with the following points:

1. Through a series of false-alarm probability statistical tests, we have shown that there exists a statistically significant peak in the BiSON SMMF residuals

spectrum which is located near the theoretical frequency of the $l = 2 = m$ r mode.

2. By modelling the peak as a Lorentzian profile we find that the peak has a central frequency of 550 ± 19 nHz (i.e. located ~ 9.2 nHz from the theoretical frequency), a line-width of $5.2^{+4.9}_{-2.8}$ nHz, and an amplitude of $\sim 27.1^{+7.9}_{-5.9}$ mG. This profile is within the upper limit for the amplitude of the $l = 2 = m$ r mode and the life time implied by the line-width is on the order of 1–2 years, which is in agreement with the observations by [Löptien et al. \(2018\)](#) and [Liang et al. \(2019\)](#).
3. Through the analysis of simulated data and hemispheric observations of the SMMF, we have shown that we should expect to see a prominent mode at the theoretical frequency, and not a split mode due to the effect of the B_0 variation, which supported the investigation that the peak may be the $l = 2 = m$ r mode.
4. By comparing the power spectrum of the SMMF observed by BiSON, to those of WSO and SDO/HMI, we have shown that the observed, statistically significant peak is not manifested in either the WSO or SDO/HMI spectra, therefore ruling it highly unlikely that the observed peak in the BiSON spectrum is the $l = 2 = m$ r mode.

As we collect more observations of the SMMF using BiSON, the frequency resolution of the power spectrum increases. An obvious next step in this work is to collect more observations of the SMMF with BiSON, to further investigate if this suspected mode remains resolved, or whether it diminishes into the noise.

Bibliography

- Appourchaux T., 2004, [A&A](#), 428, 1039
- Barnes a. W. T., et al., 2020, [ApJ](#), 890, 68
- Basu S., Chaplin W. J., 2017, Asteroseismic Data Analysis: Foundations and Techniques
- Beck J. G., 2000, [Solar Physics](#), 191, 47
- Bose S., Nagaraju K., 2018, [The Astrophysical Journal](#), 862, 35
- Brookes J. R., Isaak G. R., Raay H. B. v. d., 1976, [Nature](#), 259, 92
- Brookes J. R., Isaak G. R., van der Raay H. B., 1978, [Mon Not R Astron Soc](#), 185, 1
- Brown T. M., Christensen-Dalsgaard J., Dziembowski W. A., Goode P., Gough D. O., Morrow C. A., 1989, [The Astrophysical Journal](#), 343, 526
- Chaplin W. J., et al., 1996, [Solar Physics](#), 168, 1
- Chaplin W. J., Dumbill A. M., Elsworth Y., Isaak G. R., McLeod C. P., Miller B. A., New R., Pintr B., 2003, [Mon Not R Astron Soc](#), 343, 813
- Chaplin W. J., Elsworth Y., Isaak G. R., Miller B. A., New R., Pintr B., 2005, [Mon Not R Astron Soc](#), 359, 607
- Chaplin W. J., Elsworth Y., New R., Toutain T., 2008, [Monthly Notices of the Royal Astronomical Society](#), 384, 1668
- Dacie S., Dmoulin P., Driel-Gesztelyi L. v., Long D. M., Baker D., Janvier M., Yardley S. L., Prez-Surez D., 2016, [A&A](#), 596, A69
- Davies G. R., Broomhall A. M., Chaplin W. J., Elsworth Y., Hale S. J., 2014, [Monthly Notices of the Royal Astronomical Society](#), 439, 2025
- Dumbill A. M., 1999, PhD thesis, School of Physics and Space Research, University of Birmingham
- Elsworth Y., Howe R., Isaak G. R., McLeod C. P., Miller B. A., van der Raay H. B., Wheeler S. J., New R., 1995a. p. 392, <http://adsabs.harvard.edu/abs/1995ASPC...76..392E>
- Elsworth Y., Howe R., Isaak G. R., McLeod C. P., Miller B. A., New R., Wheeler S. J., 1995b, *Astronomy and Astrophysics Supplement Series*, 113, 379

- Foreman-Mackey D., Hogg D. W., Lang D., Goodman J., 2013, [Publications of the Astronomical Society of the Pacific](#), 125, 306
- Garca R. A., et al., 1999, *Astronomy and Astrophysics*, 346, 626
- Hale S. J., Howe R., Chaplin W. J., Davies G. R., Elsworth Y., 2016, [Solar Physics](#), 291, 1
- Hanasoge S., Mandal K., 2019, [The Astrophysical Journal Letters](#), 871, L32
- Handberg R., Campante T. L., 2011, [Astronomy & Astrophysics](#), 527, A56
- Harvey K. L., Zwaan C., 1993, [Solar Physics](#), 148, 85
- Hathaway D. H., Choudhary D. P., 2008, [Sol Phys](#), 250, 269
- Hathaway D. H., Upton L. A., 2020, arXiv e-prints, 2006, arXiv:2006.06084
- Howard R. F., 2001, in , *The Encyclopedia of Astronomy and Astrophysics*. IOP Publishing Ltd, [doi:10.1888/0333750888/2297](#), [http://eaa.crcpress.com/0333750888/2297](#)
- Howe R., 2009, [Living Reviews in Solar Physics](#), 6
- Howe R., et al., 2020, [Mon Not R Astron Soc Lett](#), 493, L49
- Kotov V. A., 2008, [Astron. Rep.](#), 52, 419
- Kotov V. A., 2012, [Bull.Crim. Astrophys. Observ.](#), 108, 20
- Kutsenko A. S., Abramenko V. I., Yurchyshyn V. B., 2017, [Sol Phys](#), 292, 121
- Lanza A. F., Gizon L., Zaqarashvili T. V., Liang Z.-C., Rodenbeck K., 2019, [A&A](#), 623, A50
- Li K. J., Yun H. S., Gu X. M., 2001, [AJ](#), 122, 2115
- Liang Z.-C., Gizon L., Birch A. C., Duvall T. L., 2019, [A&A](#), 626, A3
- Löptien B., Gizon L., Birch A. C., Schou J., Proxauf B., Duvall T. L., Bogart R. S., Christensen U. R., 2018, [Nature Astronomy](#), 2, 568
- Lund M. N., Chaplin W. J., Hale S. J., Davies G. R., Elsworth Y. P., Howe R., 2017, [Mon Not R Astron Soc](#), 472, 3256
- Maunder E. W., 1904, [Mon Not R Astron Soc](#), 64, 747
- McIntosh S. W., et al., 2014, [ApJ](#), 792, 12
- McIntosh S. W., Leamon R. J., Egeland R., Dikpati M., Fan Y., Rempel M., 2019, [Sol Phys](#), 294, 88
- Plachinda S., Pankov N., Baklanova D., 2011, [Astronomische Nachrichten](#), 332, 918
- Rossby C.-G., Collaborators 1939, [J Mar Res](#), 2, 38
- Salvatier J., Wiecki T. V., Fonnesbeck C., 2016, [PeerJ Comput. Sci.](#), 2, e55

- Scherrer P. H., Wilcox J. M., Howard R., 1972, [Sol Phys](#), 22, 418
- Scherrer P. H., Wilcox J. M., Kotov V., Severnyj A. B., Severny A. B., Howard R., 1977a, [Solar Physics](#), 52, 3
- Scherrer P. H., Wilcox J. M., Svalgaard L., Duvall Jr. T. L., Dittmer P. H., Gustafson E. K., 1977b, [Solar Physics](#), 54, 353
- Schrijver C. J., Harvey K. L., 1994, [Solar Physics](#), 150, 1
- Severny A. B., 1971, [Quarterly Journal of the Royal Astronomical Society](#), 12, 363
- Snodgrass H. B., 1983, [The Astrophysical Journal](#), 270, 288
- Stancik A. L., Brauns E. B., 2008, [Vibrational Spectroscopy](#), 47, 66
- Strohmayer T., Mahmoodifar S., 2014, A Neutron Star Oscillation Mode During a Superburst, <https://slideplayer.com/slide/10313230/>
- Svalgaard L., Wilcox J. M., Scherrer P. H., Howard R., 1975, [Sol Phys](#), 45, 83
- Thomas A. E. L., et al., 2019, [Mon Not R Astron Soc](#), 485, 3857
- Wilson P. R., 1994, [Solar and Stellar Activity Cycles](#). Cambridge Astrophysics, Cambridge University Press, Cambridge, [doi:10.1017/CBO9780511564833](https://doi.org/10.1017/CBO9780511564833), <https://www.cambridge.org/core/books/solar-and-stellar-activity-cycles/49EFD2ED430403044DEB7B7177F77DAF>
- Wu C. J., Usoskin I. G., Krivova N., Kovaltsov G. A., Baroni M., Bard E., Solanki S. K., 2018, [A&A](#), 615, A93
- Xiang N. B., Qu Z. N., 2016, [AJ](#), 151, 76
- Xie J. L., Shi X. J., Xu J. C., 2017, [The Astronomical Journal](#), 153, 171
- Zwaan C., 1981, [NASA Special Publication](#), 450
- van Driel-Gesztelyi L., Green L. M., 2015, [Living Rev. Sol. Phys.](#), 12, 1